Mutations in Fibronectin Dysregulate Chondrogenesis in Corner Fracture Type Spondylometaphyseal Dysplasia

Neha E. H. Dinesh[1], Justine Rousseau[2], Deane F. Mosher[3], Mike Strauss[1], Jeannie Mui[5], Philippe M. Campeau[2]*, Dieter P. Reinhardt [1,4]*

1. Faculty of Medicine and Health Sciences, Department of Anatomy and Cell Biology, McGill University, Montreal, QC, Canada
2. Centre Hospitalier Universitaire Sainte-Justine Research Center, Montreal, QC, Canada
3. Departments of Biomolecular Chemistry and Medicine, University of Wisconsin, Madison, WI, USA
4. Faculty of Dental Medicine and Oral Health Sciences, McGill University, Montreal, QC, Canada
5. Facility for Electron Microscopy Research of McGill University, Montreal, QC, Canada

*Co-senior authors

Corresponding author: Dr. Dieter P. Reinhardt, Department of Anatomy and Cell Biology, McGill University, 3640 University Street, Montreal, Quebec, H3A 0C7, Canada. Phone: +1 514.398.4243. E-mail: dieter.reinhardt@mcgill.ca

Keywords: Fibronectin, Skeletal Dysplasia, Chondrogenesis, Stem Cells, Differentiation

Abstract

Fibronectin (FN) is a key extracellular matrix glycoprotein indispensable for the development and function of major vertebrate organ systems. Autosomal dominant FN mutations cause corner fracture-type spondylometaphyseal dysplasia (SMDCF). However, the molecular pathomechanisms underlying this pathology are not known. Here, we have employed patient-derived induced pluripotent stem cells (iPSCs) as an SMDCF cell culture model to investigate the consequences of FN mutations in mesenchymal stem cells (MSCs) and differentiated cartilage-producing chondrocytes. The FN mutations impaired protein secretion from MSCs leading to significant accumulation of FN within the cells and strong reduction of FN in the extracellular matrix. Analyses of plasma samples from SMDCF patients showed a similar reduction in circulating FN. In mutant MSCs, FN accumulated in ribosome-covered intracellular vesicles originating from the rough endoplasmic reticulum and transitioning into lysosomes. These lysosomal vesicles were not cleared from the cytosol. Accumulation of intracellular FN elevated cellular stress markers and altered mitochondrial structure. Bulk RNA sequencing analysis revealed a specific transcriptomic dysregulation of the patient cells relative to controls. Analysis of MSC differentiation into chondrocytes showed impaired mesenchymal condensation for the mutant cells with significant reduction of key chondrogenic markers and impaired cell proliferation. FN mutant cells also displayed alterations in FN splice variants under chondrogenic stimuli. Additionally, FN mutant cells showed significantly downregulated expression of transforming growth factor beta-1 (TGFβ1), a key chondrogenic factor essential for mesenchymal condensation. Exogenous supplementation of FN or TGFβ1 promoted MSC condensation in the mutant cells. Together, the data demonstrate the cellular consequences of SMDCF-causing FN mutations on stem cells and the molecular pathogenic pathways leading to altered chondrogenesis.

Significance /Highlights

- SMDCF-causing mutations in fibronectin impair protein secretion in iPSC-derived mesenchymal stem cells.
- Mutant fibronectin and ER protein folding chaperones are directly exported from the rough endoplasmic reticulum into vesicles covered with ribosomes, which transition into lysosomes.
- These vesicles massively accumulate within the cytosol.
- Mutations in fibronectin impair mesenchymal condensation of MSCs and their differentiation into chondrocytes.
- Exogenous addition of purified fibronectin or TGFβ-1 improves mesenchymal condensation of the mutant stem cells.

Introduction

Fibronectin (FN) is a master extracellular matrix organizer that mediates pivotal roles in regulating cellular and matrix associated processes essential for development of vertebrates (1-5). In humans, FN is encoded by the 75kb fibronectin gene *FN1* located on chromosome 2 (6), that gives rise to the ~8kb transcribed premature FN mRNA. This mRNA undergoes extensive alternative splicing of exons coding for three type III domains, the extra domains A and B (EDA and EDB) and the variable domain (V) to produce 27 known transcripts (7).The various FN isoforms are critical determinants of physiological and pathological processes associated with major organ systems, such as embryonic development, neuronal patterning, development and maintenance of lungs, mammary glands, blood vasculature, in fibrosis, cancer and others (8-11). FN is secreted from cells as a 440kDa dimer linked via intramolecular disulfide bonds at the C-terminal end. Structurally, each of the 220 kDa FN monomers are composed of tandem arrays of three distinct types of domains, the type I domains (FNI1–12), type II domains (FNII1–2), and type III domains (FNIII1–15) (12). Global deletion is embryonically lethal in the *Fn1*$^{-/-}$ mouse model with severe defects in developmental patterning, presence of neural tube kink, abnormal mesoderm development, reduced embryo size, and severe growth retardation (13). Another mutant mouse model with inactivation of the FN RGD integrin binding motif (FN$^{RGE/RGE}$) displayed similar defects (14). Additionally, these mice displayed shortening of the posterior trunk and absence of limb buds during early embryogenesis (14). Mutations in FN were first reported in 2008 leading to glomerulopathy with fibronectin deposits (GFND)(OMIM #601894) (15). Following which we and others reported heterozygous autosomal dominant mutations in *FN1* that cause a rare form of skeletal dysplasia termed as "corner fracture" type spondylometaphyseal dysplasia (SMDCF) (OMIM #184255) (7, 16-18). Affected SMDCF patients suffer from visible clinical implications such as short stature and overall growth defects, severe scoliosis, coxa vara, abnormal ossification of metaphyses, and presence of vertebral anomalies (16). Notably, these FN mutations only affect the skeletal system in SMDCF patients but not in any other organ system.

Skeletal development in humans begin during embryogenesis when undifferentiated MSCs condense together to form a cartilage anlagen, which eventually remodels during embryonic growth to give rise to the appendicular skeleton by endochondral ossification (19). This is a highly orchestrated process and perturbations in endochondral ossification due to genetic mutations lead to skeletal abnormalities and dysplasias (19, 20). FN and several other ECM proteins are key components of the developing growth plate and are involved in regulation of mesenchymal condensation and endochondral ossification (19). FN is highly expressed in mesenchymal limb buds and during MSC condensation (21). A previous study reported that assembled FN promoted MSCs to condense and a transient knockdown of FN in MSCs impaired cell condensation (22). Additionally, FN promoted chondrogenesis in several other *in vitro* studies and is also implicated to have role in cartilage associated pathologies (for review see (7)). However, its exact functional role during MSC to chondrocyte differentiation, skeletal development, and growth, as well in the pathomechanism underlying SMDCF remains poorly understood.

The aim of the present study is to investigate the molecular mechanism underlying FN mutations that cause SMDCF. We have employed SMDCF patient based induced pluripotent stem cells (iPSCs) and iPSC derived MSCs and chondrocytes. We have identified that mutations in FN cause a spectrum of cellular and matrix associated defects in FN mutant cells that impair mesenchymal condensation of stem cells leading to dysregulated chondrogenesis. We have also identified the prechondrogenic regulator TGFβ1 as an essential player in this mechanism.

Results

Generation of a cell culture SMDCF model system

To investigate the molecular consequences of heterozygous FN mutations on MSC function and differentiation, we generated a cell culture SMDCF model system. Skin fibroblasts obtained from skin punch biopsies of two SMDCF patients with *FN1* mutations c.367T>C (FN_{C123R}) and c.693C>G (FN_{C231W}) and from an unaffected individual **(**donor details in **Supp Figure 1A)** were used to generate iPSCs which were further differentiated into MSCs and chondrocytes based on the experimental setup **(Figure 1A).** The number, choice of mutations, age, sex, and race of the donor cells included in the study are based on the availability of the rare patient samples. In a baseline characterization, over 90% of cells for all iPSC groups showed strong expression of the pluripotency markers SOX2, NANOG, C-MYC, and OCT4 **(Figure 1B).**
Sanger sequencing was performed on the cDNA samples of patients and control to confirm the FN mutations. FN_{C123R} mutant cells showed a heterozygous peak at nucleotide position c.367T>C confirming the FN mutation p.Cys123Arg, and FNC231W cells showed heterozygous peaks at nucleotide position c.693C>G confirming the FN mutation p.Cys231Trp in these cells **(Figure 1C).** After differentiation of the iPSCs into MSCs, over 95% of the differentiated cells for all cell groups were positive for both CD73 and CD105 and were 100% negative for the undifferentiated cell marker TRA-1-60 **(Figure 1D)**.

Secretion of FN in mutant cells is impaired leading to intracellular accumulation in vesicular structures

We previously generated recombinant mutant FN in HEK293 cells which exhibited impaired protein secretion (16). This prevented structural analysis of mutant FN. Therefore, we now employed *in silico* structure prediction tools (Alphafold2.0, PyMOL2) to compare the known FN type I (FNI) domain structure to computationally predicted mutant FN structures for FN_{C123R} and FN_{C231W}.The extent of structural differences were measured in root mean square deviation (RMSD) of atomic positions of superimposed structures. The more the RMSD values deviate from 0, the larger the structural changes. SMDCF relative to the WT FNI domains, FNI-2_{C123R} and FNI-5_{C231W} both showed subtle changes in the overall conformation of the predicted mutant domains, with low RMSD values of 0.73 Å and 0.82 Å respectively **(Figure 2A).** Minor alterations were observed upon comparison of the two adjacent domains, FNI-3 (RMSD: 0.43 Å) and FNI-4 (RMSD: 0.46 Å) **(Figure 2A).** We analyzed 7 additional SMDCF causing FN mutations and obtained similar results with RMSD values ranging from 0.23-0.91 Å for the affected FNI domains and RMSD values of 0.05-0.458 Å for adjacent domains **(Supp Figure 1B,C).** However, it is important to note that 8 out of these 9 SMDCF mutations affect cysteine residues and hence disrupt intramolecular disulfide bonds that are essential for maintaining the domain structural integrity and stabilization required for protein folding and secretion, function, and interactions.

Previous work from us and others demonstrated impaired secretion of mutant FN in HEK293 cells and in skin fibroblasts (16-18). We therefore analyzed secretion and assembly of FN in the iPSC-based model system. All stem cells were cultured in serum free conditions, hence the FN analyzed by immunostaining exclusively represents cellular FN isoforms. Immunostaining for FN in both MSCs and chondrocyte pellets of control cells showed the expected arrangement of FN fibers in the matrix **(Figure 2B)**. However, in both mutant cells a significant reduction in the assembled FN was noted under the two differentiated conditions **(Figure 2B).** No alterations in the synthesis of FN were observed between control and mutant MSCs **(Figure 2C)**. Immunoblotting of intracellular FN from cell lysates and the secreted FN from culture media of control and mutant MSCs showed intracellular FN accumulation in the mutant cells with reduced levels of secreted FN outside the cells (**Figure 2D-F**). We also tested the levels of the circulating plasma FN (pFN) in the SMDCF individuals by immunoblotting of blood serum samples compared to an unaffected individual (**Figure 2G**). Both individuals with the SMDCF mutations showed a reduction in the levels of pFN in serum. Together, the

data demonstrate that FN mutations leading to SMDCF result in reduced secretion of both cellular and plasma FN.

Since FN is known to promote cellular proliferation, we next analyzed the number of cells positive for the proliferative marker Ki-67 **(Figure 2H,I).** It was previously reported that skin fibroblasts from an individual with a p.C97W mutation in FNI-2 had no obvious defects in cellular proliferation rate (18). However, in our study we observed for FN_{C123R} and FN_{C231W} a significant reduction of Ki-67 positive stem cells **(Figure 2H,I)**. Considering the difference in cell types and the type of amino acid substituted in the specific domains, the functional consequence of these mutations may therefore differ in stem cell versus other cell types. We also analyzed the forward scatter (FSC) versus side scatter (SSC) spectra of cells in flow cytometry and we observed that both mutant cell groups had higher SSC distribution relative to the control cells **(Figure 2J).** This means that the FN mutants have increased intracellular complexity which leads to more scattering of the light, presumably by intracellularly accumulated FN.

To obtain insight into the intracellular arrangement of the retained FN, we performed transmission electron microscopy (TEM) on control and mutant MSCs **(Figure 3A-C)**. The control MSCs showed normal organization and structure of various cellular organelles such as mitochondria, rough endoplasmic reticulum (RER), and golgi apparatus (**Figure 3AI-III**). In contrast to the control cells, FN_{C123R} and FN_{C231W} exhibited numerous dense intracellular vesicles **(Figure 3B,C; arrowheads)**. These vesicles are coated with particles of ~20-30 nm in size consistent with the size of ribosomes, suggesting that these vesicles are originating from the RER and retain the misfolded mutant FN **(Figure 3B,C; arrowheads).** Frequently, the extended RER bulges out apparently forming the round vesicles containing the dense material **(Figure 3BIII and CIII; arrowheads)**. Quantification of the vesicles showed a size range between 0.04-30.91um^2 with an average size of 0.52um^2 for FN_{C123R} and between 0.08-70.66 um^2 and average size of 1.487 um^2 for FN_{C231W} (**Figure 3D,E**). FN_{C123R} MSCs had a relatively higher number of vesicles but with an overall a smaller size distribution. Majority of these vesicles were up to 1um^2 in size, covering 47.3% of total area, and larger sized vesicles with size up to 30um^2 contributed to only lesser total cell area (4.2%) **(Figure 3D)**. Whereas in the FN_{C231W} mutant cells, larger sized vesicles with sizes ranging from 35-75um^2, contributed to 27.7% of the total cell area. **(Figure 3E)**. In some FN_{C231W} MSCs it was noted that these dense structures lost their vesicular like conformation and expanded to over 50% of the entire cells **(Figure 3CI; black arrowheads)**. Presumably, the smaller vesicles fuse over time into the larger dense structures. The presence of ribosomes around these vesicles and the numerous instances of RER-like projections extending into these vesicles suggests that the misfolded mutant FN is translocated into these dense vesicle-like structures originating from the RER.

To determine whether the vesicles in mutant cells contained FN exported from the secretory pathway, we performed 12 nm immunogold labelling for FN on both control and FN mutant cells **(Figure 4)**. In control samples, we observed FN labelling only in extracellular spaces on FN fibers, but not within the cells **(Figure 4A; arrowheads)**. In the two FN mutant cells, the gold particles were prominently and uniformly present within the numerous intracellular vesicles of all sizes **(Figure 4B,C; arrowheads)**. The gold labels were irregular without any ordered pattern. The no primary antibody controls showed the absence of gold labels, validating the specificity of the antibody against FN **(Figure 4A-C; left panel).** These data demonstrate that FN is intracellularly retained in the SMDCF mutant cells in numerous unknown vesicular like structures that fills up these cells across the cellular cytoplasm.

Misfolded mutant FN is exported directly from rough endoplasmic reticulum to lysosome in FN mutant cells

Since the TEM data showed that the vesicles in FN mutants are covered by ribosomes and appear to be arising from the RER, we next tested a series of ER and intracellular vesicle and organelle markers in the MSCs using super resolution structured illumination microscopy (23, 24)

We first analyzed the abundant ER chaperone BIP/GRP78, a member of the heat shock protein 70 family, which assists in protein folding and mediates retention of misfolded proteins (25, 26). In the control MSCs we observed a punctate BIP staining throughout the cell cytoplasm **(Figure 5A)**. However, in the two FN mutants, a strong positive staining for BIP was observed in the FN-containing vesicles **(Figure 5A)** with a significant increase in overall BIP levels **(Figure 5B)**. Similar results were obtained for HSP47, which is another ER resident chaperone that interact with ECM proteins in the secretory pathway facilitating protein folding **(Figure 5C,D)** (27). FN positive vesicles in both FN_{C123R} and FN_{C231W} MSCs were also positive for HSP47 **(Figure 5C)** and had significantly higher levels of HSP47 per cell **(Figure 5D).**

The presence of ribosomes on the surface of the vesicular structures was validated by staining with antibodies against the 40S ribosomal subunit marker RPS6 (28). Control MSCs displayed a dispersed ribosomal staining throughout the cytoplasm. The mutant cells on the other hand showed predominant localization of the RPS6 around the surface of the FN containing vesicles **(Figure 5E).** Further, we performed immunostaining of several vesicle and intracellular organelle markers **(Figure 5F).** The FN containing vesicles in mutants were negative for endocytic vesicle markers RAB5 (29), an early endocytic vesicle marker and RAB7 (30), which is a late endocytic vesicle marker **(Figure 5F).** Further, these vesicles were also found to be negative for autophagy marker LC3 and additionally, no apparent changes in the structure of Golgi apparatus were observed as analyzed with marker GM103 **(Figure 5F)**. However, the FN accumulating vesicles were positive for lysosome associated membrane protein 1 (LAMP1) and both mutant cells showed higher levels of LAMP1 per cell **(Figure 5G,H)**. We further confirmed these findings by analyzing an additional lysosomal marker ATG5 (31), which demonstrated a similar staining pattern in these intracellular vesicles of the SMDCF cells **(Figure 5I).** These data suggest that in the FN mutant cells, the misfolded FN along with ER chaperones are exported directly from the RER into the transient vesicles of variable sizes, budding out of the RER that are marked with ribosomes. These vesicles eventually are believed to transition into lysosomes presumably to degrade the accumulating mutant FN.

FN mutants exhibit dysregulation of the transcriptome during chondrogenesis

To understand whether the increasing accumulation of the described vesicles within the mutants cells and the lack of FN in the mutant cell matrix affected the overall cellular transcriptome in SMDCF, we next performed bulk RNA-sequencing analysis (RNAseq) on the control and FN mutants in the MSC stage as well as after 21 d chondrogenic differentiation **(Supp Figure 2)**. Comparison of differentiated control chondrocytes to control MSCs showed an upregulation of many more genes (2549) than in downregulated genes (1359) **(Supp Figure 2A)**. This is expected as cells may require the cellular machinery to facilitate differentiation (32). In contrast, comparing the FN mutant cells either at the MSC stage or the differentiated chondrocyte stage with control cells showed a consistent pattern of more downregulated than upregulated genes **(Supp Figure 2B,C)**. At the MSC stage there are 514-850 more genes and at the chondrocyte stage 2112-2150 more genes downregulated in the mutant cells versus control cells. The higher number of downregulated genes in the latter stage shows that the effect becomes more pronounced in the mutants when subjected to chondrogenic differentiation. This suggests that the overall gene expression machinery progressively became downregulated in the two mutants during chondrogenesis, possibly due to failure of the cells to undergo cellular differentiation.

We then analyzed various subsets of gene groups to identify the cellular processes altered in the mutants. We first analyzed HSP groups (*HSP40, HSP70* and *HSP90*) of protein folding chaperones and we noted the most pronounced effects in the HSP40 family of genes **(Figure 6A-C)** with a significant increase in 18 to 19 genes for FN_{C123R} and FN_{C231W} chondrocytes **(Figure 6B,C).** These family of chaperones are critical for facilitating protein folding, unfolding, translation, translocation, degradation, and prevention of misfolded protein aggregates (33). The significant increase in these heat shock genes in the two SMDCF groups could be a driving response to the accumulating misfolded mutant FN within these cells. These cells presumably

attempt to correctly fold the mutant FN to facilitate its secretion and relieve the protein build-up within these cells. Additionally, we analyzed the small and large ribosomal subunit markers **(Figure 6D-F)**. Even though the global gene count is remarkably downregulated in the mutant cells, we observed a significant upregulation of the two ribosomal subunit genes for both FN_{C123R} and FN_{C231W} **(Figure 6E,F)**. This suggests that the mutant cells are synthesizing more ribosomal proteins to support the formation of numerous ribosomes that cover the FN-containing vesicles in both mutant cells. Since the two analyzed FN mutations affect cysteine residues and thus disrupt a disulfide bond in FN type I domains leading to a reactive free cysteine residue, we analyzed the gene family of protein disulfide isomerases (PDIs) **(Supp Figure 3A-C)**. The disulfide isomerases (DI) are enzymes that are capable of scanning proteins for misfolded regions and then oxidize, reduce, or isomerize the disulfide bonds of the affected polypeptides to facilitate proper disulfide bond formation and thus protein folding. Additionally, these enzymes can promote misfolded protein degradation (34, 35). Both FN_{C123R} and FN_{C231W} showed dysregulation in most of the disulfide isomerase enzymes and this increase in DIs was more pronounced for the FNC123R mutant (**Supp Figure 3B,C)**.

Misfolded proteins accumulating in cells often induce ER stress responses, and we noted a significant increase in some of the key cellular stress markers in the two mutant cell groups **(Figure 7A)**. Both FN_{C123R} and FN_{C231W} showed increased levels of *HSPA5* (codes for protein BIP), *ATF6* and *Calnexin* **(Figure 7A)**. The FN mutants also displayed high levels of *EIF2A* **(Figure 7A),** which is a protein translation initiator factor and in case of misfolded proteins, will attenuate global protein translation, as well as initiate cellular stress response (36). Additionally, both mutant groups exhibited increased expression of the ER degradation enhancing α-mannosidase-like proteins, *EDEM 2* and *3,* which are known key players in facilitating ER associated degradation of misfolded proteins (ERAD) and facilitating cellular resistance to ER stress (37, 38) **(Figure 7A)**.

All of these data together showed that the mutations in FN induced protein misfolding in the secretory pathway of the SMDCF stem cells that results in cellular stress responses and the attempt of cells to rectify the misfolding through protein folding chaperones. The failure of correct folding of FN results in the translocation of mutant FN from ER to transient vesicles arising from the RER which eventually transitions into lysosomes.

FN mutants have reduced gene expression profiles for FN cell receptors

FN utilizes several integrins (e.g. α5β1,αvβ1, αvβ5, αvβ3, α4β1, α3β1) and heparan sulfate proteoglycans (e.g. syndecan (SDC) 2 and 4) as cell surface receptors that facilitate interaction with cells (39). Assembly of FN depends on the interaction with integrins and syndecans, and presence of these receptors have been previously reported to be essential for FN assembly (40-42). Additionally, FN increases on the gene and protein level during chondrogenesis and assembled FN is essential for stem cell condensation (22). Hence, we analyzed the expression level of relevant integrins and syndecans in the RNAseq dataset. Differentiated control chondrocytes versus undifferentiated MSCs showed a significant increase in SDC4 and all other relevant SDCs and integrins, except ITGB1 and ITGA4 **(Figure 7B)**. On the other hand, the two mutant FN_{C123R} and FN_{C231W} chondrocytes showed a significant and consistent downregulation of most syndecans and integrins **(Figure 7B)**. A similar downregulation of the two receptor groups were observed when mutant MSCs were compared to control MSCs **(Figure 7C)**.

FN mutants are characterized by altered mitochondrial structure

The mitochondrium is a key functional organelle that maintains cellular metabolism, homeostasis, and differentiation. They form a structural and functional network with the ER and 20% of the mitochondrial membranes are in direct association with the ER (43, 44). ER stress due to damage or accumulation of misfolded proteins often lead to altered mitochondrial metabolism and function (45). Since the FN mutants displayed elevated ER stress, we evaluated the mitochondrial structure through TEM in control and mutant MSCs **(Supp Figure 4A).** Control MSCs displayed normal mitochondria size and distribution (**Supp Figure 4AI).**

In both FN_{C123R} and FN_{C231W} MSCs, the mitochondria appeared damaged with less regular mitochondrial cisternae, and the majority of the mitochondria were elongated and swollen **(Supp Figure 4AII,III)**. Additionally, we analyzed the mitochondrial structure using the Mitotracker Deep Red FM dye **(Supp Figure 4B).** Control MSCs displayed a perinuclear staining, whereas the mitochondria in the FN mutants appeared as elongated structures distributed throughout the cytoplasm (**Supp Figure 4B; arrowheads).** We also noted an overall increase in cell size in these stainings for FN_{C123R} and FN_{C231W} which is characteristic to the FN mutants. The RNAseq data set showed in control cells upon MSC to chondrocyte differentiation an overall downregulation of key mitochondrial markers **(Supp Figure 3D).** However, in the FN mutant cells, induction of chondrogenesis resulted in significant upregulation of mitochondrial markers relative to the controls chondrocytes **(Supp Figure 3E,F).** To evaluate if the structural change in mitochondria also alters their function in the SMDCF cells, we analyzed mitochondrial membrane potential and the ATP/ADP ratio **(Supp Figure 4C-E)**. However, these aspects did not change between mutant and control cells.

Mutations in FN impair mesenchymal condensation and chondrogenesis in FN mutant cells

Cell culture studies have shown that assembled FN is essential for MSCs to undergo cellular condensation, and a transient knockdown of FN or inhibition of FN assembly halted mesenchymal condensation (46). We therefore analyzed the mesenchymal condensation potential of the iPSC-derived FN mutant stem cells using the 3D micromass culturing (47, 48) and progress of condensation was determined in terms of the area of micro mass (49-52) wherein successfully condensing micromass show reduced area **(Figure 8)**. The control MSCs began to condense within the first 12 h and formed a condensed micromass by 24 h. Condensation of the FN_{C123R} and FN_{C231W} MSCs, however, remained as a large cluster of cells at the same time points and formed a full micromass by 6 d demonstrating delayed condensation **(Figure 8A).** Quantification of these micromasses at 6 d (areas in 2D) showed larger areas for the mutant micromasses than for the control, confirming altered MSC condensation **(Figure 8B).** To analyze differentiation into chondrocytes, we employed the conventional 3D pellet culturing method for 21 d (48). Following chondrogenic differentiation, we analyzed deposition of the chondrogenic marker collagen type II and FN by immunostaining **(Figure 8C-D)**. Control micromasses showed high levels of collagen type II which mostly co-localized with FN. On the contrary, the two mutant micromasses showed virtually little to no collagen type II deposition and a significantly reduced expression of *COL2A1* mRNA **(Figure 8E)**.

To further validate these findings, we analyzed the RNAseq data for other chondrogenic marker expression levels in the MSC versus chondrocyte stage. We focused on proteoglycans, matrix metalloproteases (MMPs), matrix markers, transcription factors, cell surface markers and growth factors **(Supp Figure 5A,B and Figure 9A,B)**. Differentiated control chondrocytes showed a consistent and significant increase in over 30 chondrogenic markers relative to undifferentiated control MSCs, confirming effective differentiation into chondrocytes **(Supp Figure 5A,B)**. On the contrary, majority of those chondrogenic markers were significantly downregulated in FN_{C123R} and FN_{C231W} chondrocytes relative to the differentiated control chondrocytes **(Figure 9 A,B)**. This data further substantiated the impaired chondrogenic differentiation capability of the two SMDCF mutant cell groups. Additionally, control differentiated chondrocytes showed increased expression for the FN gene, corroborating with the literature data (21, 53) **(Supp Figure 5A)**. However, mutant cells demonstrated a significant reduction in the FN expression level **(Figure 9A)**. Taken together these data confirmed that mutations in FN impair the mesenchymal condensation and differentiation of MSCs into chondrocytes in SMDCF.

Mutations in FN1 alter the FN splicing pattern in SMDCF

The *FN1* gene gives rise to 27 transcripts by alternative splicing; 13 transcripts code for various FN isoforms, 1 is a non-coding transcript, and 13 transcripts are classified as retained introns (9) **(Supp Figure 6A)**. Several cell culture studies explored the functional importance of some of these isoforms in the context of chondrogenesis and skeletal development (7); however the exact physiological relevance and role in cartilage

development remains unclear. Considering the importance of FN in stem cell differentiation and initiation of chondrogenesis, we analyzed the differential expression level of the various FN transcripts in the RNAseq data, in the control and mutant cells. We analyzed the global transcript count of the 27 transcripts in the FN_{C123R} and FN_{C231W} mutant versus control cells in MSCs and in differentiated chondrocytes, and filtered those that are significantly dysregulated between the conditions **(Supp Figure 6B,C)**. Comparison of control chondrocytes and MSCs showed significant changes in 4 FN transcripts which included the coding transcript FN1-204 (V) and three retained intron transcripts **(Supp Figure 6B)**. The two FN mutants upon chondrogenic differentiation showed dysregulation of 7-9 protein coding transcripts with inclusion of the V, EDA and/or EDB domains **(Supp Figure 6B)**. Significant changes in the same transcripts were noted for FN_{C123R} MSCs versus the control MSCs **(Supp Figure 6C)**. However, the FN_{C231W} MSCs exhibited alterations in only two *FN1* retained intron transcripts (FN1-224 and FN1-225) **(Supp Figure 6C)**. Analysis of differential expression of *FN1* transcripts in osteoarthritis (OA) lesion cartilage was published earlier this year, wherein it was shown that OA is characterized by changes in the expression of specific *FN1* transcripts that were linked to reduced GAG and collagen type II expression (54). We noted an overlap for some of these *FN1* transcripts between this study and our work (FN1-204, 209,212, 224, 225 and 227). Which altogether suggests that the splicing and expression of specific *FN1* transcripts change during cartilage associated pathologies.

Exogenous treatment with FN and TGFβ1 can rescue impaired mesenchymal condensation of FN mutant stem cells

We next analyzed the major cellular and matrix markers involved in chondrogenesis regulating pathways that are potentially dysregulated in the FN mutants. We sorted markers broadly into three major groups and analyzed those involved in TGFβ and bone morphogenetic protein (BMP) mediated signaling **(Figure 10A,B)**, fibroblast growth factor (FGF) signaling and Indian hedgehog (IHH) signaling. We noted pronounced effects in the TGFβ group of markers **(Figure 10B)**. TGFβ1 was elevated significantly in control chondrocytes versus control MSCs and was dramatically downregulated in the mutant chondrocytes versus control chondrocytes **(Figure 10A-C,arrowheads)**. TGFβ1 promotes mesenchymal condensation and chondrogenesis (55). Additionally, both FN and TGFβ1 have been reported in several studies to modulate each other in the context of chondrogenesis (7). Therefore, we focused on investigating the role of TGFβ1 in the SMDCF cells.

Cell proliferation of stem cells and chondrocytes is essential for chondrogenic differentiation and long bone growth. We noted that the FN mutant MSCs stained significantly lower for the cell proliferation marker Ki67 **(Figure 10C,E)**. We then investigated whether exogenous supplementation of recombinant human TGFβ1 (10ng/mL) or purified fibronectin (25µg/mL) in the culture medium can improve the proliferation defect. FN_{C123R} MSC showed a slight but significant increase in KI67 positive cells upon treatment with either FN or TGFβ1, but not FN_{C231W} MSCs **(Figure 10C,E)**. Further, we analyzed if supplementation of TGFβ1 and FN can rescue the mesenchymal condensation defect in the FN mutants using 3D micromass cultures. No changes were observed in control stem cell condensation upon treatment with TGFβ1 or FN. However, the FN_{C123R} and FN_{C231W} MSCs displayed a visible and quantifiable improvement in mesenchymal condensation upon addition of both TGFβ1 and FN **(Figure 10D,F)**.

As IPSC controls were limited at the beginning of our study hence most of our experiments were performed with one biological control iPSC line. However, as the iPSCs became commercially available, we validated this rescue experiment with additional sex matched iPSC controls (*GM23338, denoted as Ctrl2* and *GM23716, denoted as Ctrl3*). Ctrl2 and Ctrl3 iPSCs were cultured and validated for pluripotent markers and MSC markers upon differentiation (**Supp Figure 7A-D**). Relative to the new control cell groups, both FN mutants FN_{C123R} and FN_{C231W} displayed a significantly delayed condensation of MSCs, as marked by the increased micromass size at 6 d. This defect in condensation was rescued in the two mutants by exogenous supplementation of either FN or TGFβ1, given by the significantly reduced micromass sizes for both FN mutants under treated conditions (**Supp Figure 7E**). No alterations were observed in condensation of control cell groups upon treatment with

371 TGFβ1 or FN. Altogether, these results demonstrate that exogenous addition of TGFβ1 and FN can partially
372 rescue the stem cell condensation defect in the SMDCF mutant cells.

Discussion

FN is a vital regulator of various organ systems in embryonic and postnatal development. However, virtually nothing is known about the consequences of SMDCF-causing FN mutations on cell physiology and pathology. These are heterozygous mutations with an autosomal dominant inheritance pattern which cause severe impact on the development of the skeletal system. In the present study, we have developed an SMDCF model system using iPSCs generated from fibroblasts obtained from two previously reported SMDCF patients harboring FN mutations p.C123R and p.C231W in FNI domains at the N-terminal region of FN (16, 17). Since defects in skeletal growth and development is the predominant clinical phenotype reported in individuals with SMDCF, we differentiated the SMDCF iPSCs into MSCs and subsequently into chondrocytes to investigate the consequence of FN mutations on stem cell differentiation and chondrogenesis.

In line with previous work (16), we show with the patient-derived SMDCF MSCs, that the FN containing SMDCF mutations are not secreted and accumulate within cells. Since these are heterozygous mutations, the expected FN dimer secretion is 25% each of wild type and mutant homodimers and 50% of wild type/mutant heterodimers. However, our results show very little FN secreted by the mutant cells, suggesting that the wild type FN containing homo- and heterodimers were co-retained together with mutant FN homo- and heterodimers in the patient cells. This initiated cellular stress response, mitochondria structure alterations, and increased synthesis of protein folding chaperones such as BIP and HSP47. On the contrary, autophagy was not activated. Both analyzed mutations inevitably disrupt known disulfide bonds in the FNI-2 domain (pattern Cys1-Cys3) and the FNI-5 domain (pattern Cys2-Cys4) (16, 17, 56). Almost all other known SMDCF-causing mutations also disrupt disulfide bonds in FNI domains (16-18). AlphaFold predicted that both mutations introduce relatively minor structural changes within the mutation-containing domain as well as directly adjacent FNI domains. This is in line with previous structure predictions of p.C87F (16). The data suggests that consequences arising from a disrupted disulfide bond in an FNI domain are more relevant for the disease mechanism than any other gross structural changes within the individual FNI domains. One possible and likely consequence is that the uncoupled cysteine residue provides a reactive free sulfhydryl group that can form an aberrant disulfide bond either with other mutant or unaffected FN molecules, or with other proteins harboring free cysteine sulfhydryl groups. Both scenarios are predicted to lead to protein aggregation and misfolding (57). In addition, previous studies have reported that mutations of selected conserved residues (other than cysteines) in FNI-1 to 5 also impair FN secretion (58), because these N-terminal FNI domains act as a unit to facilitate proper folding and secretion (3, 58).

We noted in SMDCF MSCs numerous vesicles in the cytosol ranging from ~100 nm – 2 µm in diameter. These vesicles contained FN and the chaperones BIP and HSP47 and had the signature of ribosomes covering the surface. Electron microscopy showed that these vesicles bud out directly from the RER. We interpret these results as a means of the cells to clear the RER after the chaperones were unsuccessful in mediating proper FN folding. Many of the cytosolic vesicles were positive for the lysosomal markers LAMP1 and ATG5, suggesting a transition or fusion into lysosomal structures, presumably in an attempt to degrade the accumulating FN. These observations are consistent with ER-to-lysosomes-associated degradation (ERLAD). Similar cellular mechanisms have been previously reported for several pathological conditions, including the α1-antitrypsin deficiency diseases (59, 60). Misfolded α1-antitrypsin that accumulates within the RER of liver cells is directly exported from the RER to lysosomes for ER-to-lysosome associated degradation (60, 61). Another example for ERLAD comes from experiments with hyper-stimulation of the thyroid, where thyrotrophic hormone producing cells develop intracisternal granules in the RER causing the RER to dilate and transition into cisternae containing the β subunits of thyrotrophic hormone (62). These cisternae converted directly into lysosomes to facilitate protein degradation. Typically, BIP and other ER chaperones that escape the RER are retrieved in COPI vesicles via the KDEL receptor recognition system from post-ER compartments back to the ER lumen (63). However, we observed the presence of chaperones together with FN in the

422 vesicular structures in mutant SMDCF cells. Mutant FN aggregation or misfolding apparently triggered its
423 export from the RER with associated chaperones bypassing the KDEL recognition system in the Golgi
424 apparatus.
425
426 As the identified vesicles become lysosome-like structures, the expectation is that lysosomal proteases would
427 degrade the accumulating FN. However, they clearly fail to degrade the content in an efficient manner as
428 evidenced by the massive accumulation of these vesicles in the cytosol in the absence of increased FN
429 synthesis. It is possible that aggregated or misfolded FN is so densely packed and possibly cross-linked through
430 additional disulfide bonds so that lysosome resident proteases are not able to dock onto the respective
431 recognition sites and thus are not able to degrade mutant FN. This notion is consistent with our electron
432 microscopy analyses that demonstrated a rich and dense labeling of the vesicles with anti-FN antibodies.
433 Alternatively, it is possible that chaperones complexed with FN aggregates prevent lysosomal FN degradation.
434 It will be important in the future to further analyze degradation mechanisms of mutant FN in these vesicular
435 structures and to test strategies that potentially facilitate lysosomal FN degradation, for example using
436 lysosome enhancing agents (64). Interestingly, there are no reported defects in other organ systems of the
437 patients with SMDCF, while the same pathological molecular pathways should be in place in other cells. For
438 example, one would expect a liver phenotype, supported by our findings of reduced levels of circulating FN
439 in FN_{C123R} and FN_{C231W} mutant cells, suggesting impaired FN secretion from hepatocytes. Since hepatocytes
440 are specialized liver cells with enhanced ability to clear toxins and misfolded proteins, it is possible that the
441 degradation of misfolded mutant FN in those cells is more efficient, thereby preventing functional defects in
442 the liver (65).
443
444 Cell proliferation and differentiation are closely associated during cartilage development. Hence, we analyzed
445 proliferation of iPSC-derived FN mutant MSCs, demonstrating a significant reduction of stem cell proliferation
446 in the two mutant cell groups. This contrasts with a previous study, reporting the absence of proliferative
447 effects using skin fibroblasts from an SMDCF patient with a p.C97W mutation in FN (18). A possible
448 explanation is that a FN deficient matrix and/or the abnormal protein accumulation in the SMDCF cells may
449 impact stem cells differently than fibroblasts. The reduced proliferation potential of SMDCF MSCs likely plays
450 an important role in the context of pathologic chondrogenesis, as mesenchymal progenitor cells normally
451 have to undergo extensive proliferation to increase cell density and allow enhanced cell–cell contacts to
452 facilitate mesenchymal condensation (66-68), and differentiation into chondrocytes (69). FN promotes
453 cellular proliferation through integrins in various cells including chondrocytes (70). Thus, the absence of FN in
454 the ECM of SMDCF cells is likely a key contributing factor to the reduced proliferation observed in these cells.
455 We attempted to rescue this defect with exogenous supplementation of purified FN to the mutant cells which
456 led to only a small improvement of cell proliferation for FN_{C123R} but not for FN_{C231W} cells. We suspect that this
457 could be due to the reduced expression of key FN interacting integrins subunits (e.g. ITGB1, ITGB3, ITGAV)
458 observed in the FN mutants, which i) are predicted to reduce the interaction of FN with cells and ii) may affect
459 assembly of exogenously provided FN.
460
461 We demonstrated that the FN mutant stem cells display delayed condensation and impaired chondrocyte
462 differentiation marked by reduction in collagen type II at the mRNA and protein levels. This is in contrast to
463 the recently identified osteoarthritis-causing FN mutation p.C518F in the FNI-8 domain, which did not impair
464 FN secretion, but instead reduced the binding of FN to collagen type II (71). The fact that in SMDCF the
465 impaired FN secretion severely affects MSCs from differentiating into chondrocytes and expressing collagen
466 type II as well as a wide spectrum of other chondrogenic markers, demonstrates the pathologic severity of
467 the SMDCF mutations on cellular differentiation.
468
469 One of the possible reasons for the impaired chondrogenesis in SMDCF could be a reduced or altered
470 interaction of FN with integrins or syndecans, as both regulate chondrogenesis and the expression of
471 chondrogenic markers *in vivo* (14, 72, 73). Deficiency of FN in the SMDCF cell matrix, as well as reduced

472 expression of these surface receptors noted in the mutant cells could presumably disrupt FN-receptor
473 interaction efficiency in SMDCF, dysregulating chondrogenesis. Alternatively, the impaired chondrogenesis
474 could be a result of defects in TGFβ signaling, which is indispensable for regulated cartilage development (55,
475 74, 75). Both FN and TGFβ have intertwined roles in chondrogenesis(7). FN induced increased TGFβ levels and
476 signaling during chondrogenesis in several cell culture studies (76). In turn, TGFβ also promoted expression
477 of FN and differential isoform expression in chondrocyte cultures (7). In the present study, we identified that
478 TGFβ1 mRNA was significantly downregulated in the FN mutant cells when subjected to chondrogenic
479 differentiation. Whether the absence of FN in the matrix directly diminished TGFβ1 levels, or whether it first
480 impaired stem cell differentiation resulting in reduced TGFβ1 expression, or whether the altered TGFβ1 level
481 alone was the primary driver for defective chondrogenesis in the mutant cells remains to be established.
482 Nevertheless, supplementation of purified FN or active TGFβ1 partially rescued defective stem cell
483 differentiation and condensation of both FN_{C123R} and FN_{C231W} mutant cells. Based on these cell culture data,
484 supplementation with exogenous FN and TGFβ may be beneficial in the future to alleviate pathological
485 aspects in SMDCF. However, testing this hypothesis is currently hampered by the lack of a suitable SMDCF
486 mouse model.
487 In summary, the present study explores the molecular pathomechanisms underlying FN mutations that cause
488 SMDCF leading to the model outlined in **Figure 11**.
489
490 In unaffected cells under normal physiological conditions **(Figure 11A)**, FN is co-translationally translocated
491 into the ER lumen, where it undergoes dimerization, post-translational modifications, and protein folding.
492 Folded FN is sorted into transport vesicles that carry the protein from the RER to the Golgi apparatus and
493 further into secretory vesicles, which are targeted to the plasma membrane for release into the ECM. The
494 secreted compact FN dimer interacts with cell surface receptors triggering assembly into a fibrous FN network.
495 The FN matrix promotes MSCs to undergo mesenchymal condensation and chondrogenic differentiation
496 associated with increased levels of FN and TGFβ1, facilitating regulated skeleton development.
497
498 In cells harboring disease-causing SMDCF mutations **(Figure 11B)**, FN together with ER chaperones are
499 intracellularly retained inside vesicles that originate from the rough ER and transition into lysosomes. These
500 defects induce elevated cellular stress, altered mitochondrial structure, reduced cell proliferation, matrix
501 deficiency in FN, and reduced levels of TGFβ1 upon chondrogenic induction. These molecular defects affect
502 the mutant MSCs to differentiate into chondrocytes contributing to skeletal dysplasia development
503 characteristic for SMDCF.

Materials and Methods

IPSC Culture and Differentiation into Mesenchymal Stem Cells

Skin fibroblasts from SMDCF patients with FN mutations FN_{C123R} and FN_{C231W} and from an unaffected individual were used to generate induced pluripotent stem cells (IPSCs) at the core facility of CHU-Saint Justine (Montreal, Canada). Fibroblasts were reprogrammed to iPSCs with integration-free Sendai virus expressing Oct4, Sox2, Klf4, and c-Myc, using CytoTuneTM-iPSC reprograming kit (Life Technologies; Catalogue #A13780-01, A13780-02), followed by validation of the iPSC colonies by staining with antibodies for markers SSEA-4, Sox2, OCT4, and TRA1, as described previously (77). Generation and use of the patient cells was approved by Institutional Review Board (IRB) (Protocol number: MP-21-216-962, 4181). Additional control iPSCs were purchased from the Coriell Institute for Medical Research (GM23338 and GM23716). IPSCs were cultured using a feeder free method with E8 serum free essential medium (Life Technologies; Catalogue #A1517001), supplemented with antibiotic Primocin (100 µg/mL, Invivogen; Catalogue #ant-pm-2), and 2mM L-Glutamine (Stem Cell Technologies; Catalogue #07100;). Geltrex Matrix (800 µg/mL, Gibco; Catalogue #A14133-0), a reduced growth factor basement membrane matrix, was used as the coating substrate for iPSC cultures. Cells were treated with E8 medium supplemented with rock inhibitor RevitaCell supplement (Gibco; Catalogue #A2644501) for 18-24 h for post thaw recovery of cryopreserved iPSCs and during passaging. Gentle Cell Dissociation Reagent (Stem Cell Technologies; Catalogue #07174) was used for passaging the colonies. IPSCs were validated for the expression of pluripotent markers using flow cytometry outlined below.

IPSCs were differentiated into MSCs using the STEMdiff Mesenchymal Progenitor Kit (Stem Cell Technologies; Catalogue #05240;). The differentiation protocol involved treatment of IPSCs with STEMdiff Animal Component-Free (ACF) Mesenchymal Induction Medium for 4 d, followed by expansion and further culturing with MesenCult ACF medium (Stem Cell Technologies; Catalogue #05445), supplemented with 2mM L-Glutamine (Stem Cell Technologies; Catalogue #07100) for 21 d. The mesenchymal progenitor cells were tested and validated for the expression of MSC markers (see below). All MSCs were cultured on ACF Cell Attachment Substrate coated surfaces (Stem Cell Technologies; Catalogue #07130). ACF Cell Dissociation Kit (Stem Cell Technologies; Catalogue #05426) was used for passaging the MSCs for expansion and experiments. All stem cells were cultured at 37°C, 5% CO_2, 5%O_2 and 90% humidity.

Differentiation and Analysis of Mesenchymal Stem Cells in Chondrocytes

MSCs were differentiated into chondrocytes using the MesenCult-ACF Chondrogenic Differentiation Kit (Stem Cell Technologies; Catalogue #05426) comprising of MesenCult-ACF Chondrogenic Differentiation Basal Medium (Stem Cell Technologies; Catalogue #05456) and MesenCult-ACF 20× Chondrogenic Differentiation Supplement (Stem Cell Technologies; Catalogue #05457). Chondrogenic induction medium was supplemented with the 1× differentiation supplement and 2mM L-Glutamine. MSCs were differentiated either by 3D micromass culturing for 6 d for the cell condensation assay (1×10^6 cells/mL) or alternatively by 3D pellet culturing for 22 d (5×10^5 cells per micromass) in 15mL conical tubes (Corning; Catalogue #352096). All cells were cultured at 37°C, 5% CO_2, 5%O_2 and 90% humidity. Following differentiation, micromasses or pellets were either fixed with 4% paraformaldehyde (PFA) for 24 h or used directly for RNA and protein extraction. Fixed masses were paraffin embedded and sectioned at 4µm thickness for immunostaining and histological analysis.

Cell Condensation Assay

MSCs were cultured and differentiated into chondrocytes by 3D spheroid/micromass culturing technique using the Nunclon Sphera 96 well plates (Thermo Fisher Scientific; Catalogue #174927) that prevented cell adhesion to the plate surface and promoted spheroid formation for live cell condensation assays. For micromasses, cells were seeded at high density and as small microliter droplets onto culture plates. 20µL of a 1×10^6/mL cell suspension were plated per well and incubated for 1 h, followed by addition of 150µL chondrogenic induction medium. Condensation of micromasses was imaged from 1 h to 6 d using a light

553 microscope (Axiovert 40CFL) and the ZEN 2 (blue edition) software. Rescue experiments were performed by
554 supplementing the medium with either 25 µg/mL human plasma fibronectin (Millipore Sigma; Catalogue
555 #FC010) or with 10 ng/mL of human TGFβ1 (Peprotech; Catalogue#100-21). At the experimental end point at
556 6 d, post imaging the samples were fixed with 4% PFA for 1 h followed by paraffin embedding and sectioning
557 (4µm) for immunostaining and histological analysis. Images of micromasses were used for quantification of
558 total micromass area using Image J software (78)
559
560 ***Flow Cytometry***
561 IPSCs were immunostained for pluripotent markers C-MYC, NANOG, OCT4 and SOX2 and MSCs were stained
562 for CD73, CD105 and an undifferentiated IPSC marker TRA-1-60 using specific antibodies conjugated with
563 fluorophores (Supp Table 1). Cell density in each sample was maintained at 5×10^5 cells/mL for all analysis.
564 Antibody labelling and flow cytometric analysis followed standard procedures using the BD LSR Fortessa 5L
565 flow cytometer and the BD FACS Diva 8.0.2 software at the Advanced BioImaging Facility of the McGill Life
566 Sciences Complex (Montreal, Canada). The FlowJo 10.8.1 software was used for further data analysis.
567
568 ***Transmission Electron Microscopy (TEM) and Immunogold Labelling***
569 For TEM, MSCs were seeded at a density of 75,000 cells/well of Nunc Lab-Tek 8-well chamber permanox slides
570 (Thermo Fischer Scientific; Catalogue #177445) and cultured for 3 d. Cells were fixed with 2.5% glutaraldehyde
571 at 4°C overnight, washed with 0.1 M cacodylate buffer, and stained with 1% aqueous osmium tetraoxide and
572 1.5% potassium ferrocyanide for 1 h at 4°C. Counter staining was with 2% uranyl acetate for 1 h, followed by
573 embedding with Epon and sectioning (70-80nm). For immunogold labelling experiments cells were fixed with
574 4% PFA+0.05% glutaraldehyde in 0.1M sodium cacodylate buffer for 1 h and then embedded in LR white resin,
575 followed by UV light mediated polymerization in a Leica EM AFS2 embedding system. Sections were placed
576 on formvar coated mesh copper grids and immunostained with anti-human fibronectin primary antibody and
577 12 nm colloidal gold AffiniPure Donkey anti-rabbit secondary antibody (Supp Table 1). Counter staining was
578 performed as described before. Imaging was performed on a FEI Tecnai 12 120kV TEM microscope at the
579 McGill University Facility for Electron Microscopy Research Facility using a AMTV601 CCD camera.
580
581 ***Sanger Sequencing and qPCR***
582 Cells were seeded at a density of 1.5×10^5 cells/well in 6 well plates (Corning; Catalogue #3516) and cultured
583 for 3 d. Total RNA was extracted using the RNeasy kit (Qiagen; Catalogue #74104) as per the manufacturer's
584 instructions. cDNA was prepared with 0.1-1 µg of total RNA using the Protoscript First Strand cDNA Synthesis
585 kit (New England Biolabs; Catalogue #E6560L) as per the manufacturer's instructions. For real-time qPCR,
586 experiments were performed using a SYBR Select Master Mix (Applied Biosystems, Catalogue# LS4472908).
587 For sanger sequencing PCR reactions were performed using specific oligos against the target FN domains
588 (Supp Table 2) and Taq DNA Polymerase kit (ZmTech Scientifique; Catalogue #T207025) and analyzed on 2%
589 agarose gels. The amplified PCR products were extracted from the gel using the QIAquick Gel Extraction Kit
590 as per manufacturer's instructions (Qiagen; Catalogue #28704), followed by Sanger DNA sequencing of the
591 PCR products at the Génome Québec (Montreal, Canada).
592
593 ***RNA Sequencing and Data Analysis***
594 MSCs were cultured for 10 d (1.5×10^5 cells in triplicates per cell group) and chondrocyte differentiation was
595 performed for 21 d as described above. RNA was extracted using the RNeasy kit (Qiagen; Catalogue #74104)
596 as per the manufacturer's instructions. RNA samples (150 ng/µL) were analyzed at the McGill Genome Centre
597 (Montreal, Canada) for quality and integrity (RIN) using the Qubit RNA High Sensitivity Assay and TapeStation.
598 All samples were found to have high RIN values between 8.2-9.5. Ribosomal RNA was depleted and cDNA
599 libraries were prepared using 1 µg RNA per sample. Bulk RNA sequencing was performed with the Illumina
600 NovaSeq6000 system. Processing of the raw RNAseq dataset and differential gene expression analysis was
601 performed by the Canadian Center for Computational Genomics (C3G; Montreal, Canada). The Ensemble

602 GRCh38.p13 (Genome Reference Consortium Human Build 38) was used as the reference database for
603 alignment of the reads. GenPipes is the main in-house framework of the C3G used to perform major
604 processing steps (79). Adaptor sequences and low-quality score containing bases (Phred score < 30) were
605 trimmed from reads using Trimmomatic (80). The resulting reads were aligned to the genome, using STAR
606 (81). Read counts were obtained using HTSeq (82). The R package DESeq2 was used to identify differences in
607 expression levels between the groups using negative Binomial GLM fitting and Wald statistics
608 (nbinomWaldTest) (83). The R package *ashr* was used to shrink log2 fold changes in gene expression data (84).
609 All data sets in figures represent gene expression in regularized log counts (rlog counts) unless specified
610 otherwise in the figure legends. For gene group sets, the HUGO Gene Nomenclature Committee (HGNC)
611 classification was used as a reference.
612

613 ***In silico Structure Prediction***

614 Bioinformatic structure predictions were performed using the ColabFold v1.5.3: AlphaFold2 using MMseqs2,
615 a simplified version of AlphaFold v2.3.1 (85). Sequence for human fibronectin was obtained from the Uniprot
616 database (Sequence ID: P02751-15, correlating to DNA reference NM_212482.4). Structure predictions were
617 made for the FN domain type I domains 1, 2, 3, 4 and 5 using the respective sequences from P02751-15. To
618 predict structural consequences of the FN mutations FNC123R and FNC231W were introduced into the wild
619 type FN sequences. For both wild type and FN mutant domains, structures with highest ranking were analyzed
620 and selected. Structure visualization and alignment was performed using the PyMOL software (86, 87). Root
621 mean square deviation (RMSD) for alignment of mutant domain structures with the respective wild type
622 domains were obtained using the CE algorithm in PyMOL.
623

624 ***Immunoblotting***

625 For immunoblotting analysis, cells were lysed using RIPA buffer (50 mM Tris, pH 8.0, 150 mM NaCl, 0.5%
626 sodium deoxycholate, 1% Triton X-100, 0.1% sodium dodecyl sulfate) supplemented with 2% v/v protease
627 inhibitor cocktail (Roche; Catalogue #11697498001) and 1% v/v phosphatase inhibitor cocktail (Sigma-Aldrich,
628 Catalogue #P5726). Lysates were centrifuged at 180 × g for 5 min to pellet the debris and the clear lysates
629 were used for immunoblotting. Total protein concentration was determined by the BCA protein assay kit
630 (Thermo Fisher Scientific; Catalogue #23225). Total protein ranging from 20-30µg was used in a standard
631 immunoblotting procedure. All antibodies used in various experiments with the respective dilutions are listed
632 in Supp Table 1. Horse radish peroxidase-conjugated goat anti-rabbit or anti-mouse secondary antibodies
633 were incubated for 2 h at ambient temperature. Super signal chemiluminescent western blotting substrate
634 (Thermo Fisher Scientific; Catalogue #34580) was used for the developing of blots, and images were recorded
635 using the ChemiDoc MP imaging system (Bio-Rad). Band intensities were quantified with ImageJ (78) and
636 normalized to the GAPDH control.
637

638 ***Analysis of Human Plasma Samples***

639 Human plasma samples were obtained from the two SMDCF patients with the FN mutations p.C123R and
640 p.C231W, and from an unaffected individual (parent of patient with the p.C123R mutation). Plasma samples
641 were analyzed for fibronectin by immunoblotting using 0.1µL plasma sample under reducing conditions with
642 a specific anti-human FN antibody (Supp Table 1) .
643

644 ***Immunostaining and Immunofluorescence Microscopy with Apotome***

645 For indirect immunofluorescence staining, cells were plated on Nunc Lab-Tek 8-well chamber permanox slides
646 (Thermo Fischer Scientific; Catalogue #177445) at a density of 75,000 cells per well and cultured as specified
647 in the figure legends. Cells were fixed with 4% PFA or 4% PFA including 0.1% Triton X-100, depending on the
648 experimental setup, blocked with 10% v/v goat serum, and incubated overnight at 4 °C with either one or two
649 primary antibodies (raised in different species) for single or double immunostaining, respectively (Supp Table
650 1). Alexa Fluor 488 goat anti-rabbit antibody, Cy3 goat anti-mouse antibody or Cy5 goat anti-mouse antibody

were used in combination or alone as secondary antibodies (Supp Table 1). Nuclei were counter-stained with 4, 6-diamidino-2-phenylindole (DAPI) (Abcam; Catalogue #188804). An epifluorescence microscope (Zeiss; AxioImager M2) with an Orca Flash 4.0 CMOS camera was used for analysis. All images were originally in grayscale and then pseudo-colored using the Zen Pro software version 2.6 (Zeiss). Superresolution Structured Illumination Microscopy was performed using the Zeiss Apotome 2 fitted with the AxioImager M2. Apotome calibration and validation of the imaging technique was performed using 0.2µm TetraSpeck microspheres (Invitrogen; Catalogue #T7280) and Zeiss immunofluorescence calibration slides (Zeiss; Catalogue #000000-1213-943). Post processing of apotome images included phase correction and deconvolution.

Image Quantifications

Quantification of the mean fluorescence intensity of specific markers was performed by processing of the images as described previously in detail (88). Mean intensity per cell were quantified by outlining single cell area. Quantification of Ki-67 positive cells were performed using a procedure described previously (88). The number of Ki-67 positive cells was normalized to the total number of DAPI stained cells per image. Quantification of the area of micro masses in cell condensation assays were performed by outlining the micromasses using the Wacom Intuos Graphic Tablet with Stylus (Model no. CTH490AK) in ImageJ. Similarly, for quantification of area and number of intracellular vesicles from the EM micrographs, vesicles were outlined using the freehand tool in Image J with the Wacom tablet and stylus and the data was plotted as histogram using the “distribution” statistical function in the Origin Pro software.

Statistics

All data are represented as means ± standard deviation (SD) or standard error of the mean (SEM), depending on the experimental setup as indicated in the figure legends. Experiments were performed either as triplicates or quadruplets. Significance was evaluated using either Student's two tailed t-test, or one-way or two-way ANOVA post Bonferroni test as specified in each figure legend. All statistical analyses were performed using the OriginPro version 2023 software (OriginLab). Outlier analysis was performed using the Grubb's test with confidence levels set to 95%. Data with p-values ≤0.05 were considered significant and are denoted as *. Non-significance is labeled “n.s.”.

Schematic Figures

All schematics in this manuscript were prepared using the Biorender software (URL: https://app.biorender.com/)

Data Availability

The RNA sequencing data has been submitted to the NCBI's Gene Expression Omnibus database (https://www.ncbi.nlm.nih.gov/geo) and is available through GEO accession number GSE251698. All other datasets that support the findings of this study are available from the corresponding author upon request.

Acknowledgements

We express our sincere gratitude to the SMDCF patients for donating samples for this research study. Additionally, we would like to acknowledge the Facility for Electron Microscopy Research at McGill University, for their assistance with access and preparation of samples for electron microscopy. We are also grateful to the McGill Genome Centre for performing the RNA sequencing and to the Canadian Center for Computational Genomics for their assistance with the RNAseq data analysis.

Author Contributions

ND, DPR, and PC conceived the study, designed the experiments, analyzed the data, and wrote the manuscript (with critical input from all authors). ND performed the experiments. DPR and PC provided the research funds.

Competing Interests

The authors declare no competing interests.

Funding

This work was supported by the Canadian Institutes of Health Research (Grant PJT-156140 to PC and DPR), and the Fonds de recherche de Quebec (Dossier No. 291220, fellowship to ND). The funders have no role in study design, data collection and analysis, decision to publish, or preparation of the manuscript.

706 **References**

707 1. Longtin R, Birthday of a breakthrough: fibronectin research proves important, but not as originally
708 expected. *J Natl Cancer Inst* **96**, 6-8 (2004).
709 2. Goudemand M, Plasma fibronectin. *Rev Fr Transfus Immunohematol* **26**, 279-298 (1983).
710 3. Maurer LM, Ma W, Mosher DF, Dynamic structure of plasma fibronectin. *Crit Rev Biochem Mol Biol*
711 **51**, 213-227 (2015).
712 4. Sottile J, Hocking DC, Fibronectin polymerization regulates the composition and stability of
713 extracellular matrix fibrils and cell-matrix adhesions. *Mol Biol Cell* **13**, 3546-3559 (2002).
714 5. Sottile J, Hocking DC, Langenbach KJ, Fibronectin polymerization stimulates cell growth by RGD-
715 dependent and -independent mechanisms. *J Cell Sci* **113 Pt 23**, 4287-4299 (2000).
716 6. Prowse KR, Tricoli JV, Klebe RJ, Shows TB, Assignment of the human fibronectin structural gene to
717 chromosome 2. *Cytogenet Cell Genet* **41**, 42-46 (1986).
718 7. Dinesh NEH, Campeau PM, Reinhardt DP, Fibronectin isoforms in skeletal development and
719 associated disorders. *Am J Physiol Cell Physiol* **323**, 536-549 (2022).
720 8. Chen D, et al., Fibronectin signals through integrin alpha5beta1 to regulate cardiovascular
721 development in a cell type-specific manner. *Dev Biol* **407**, 195-210 (2015).
722 9. White ES, Muro AF, Fibronectin splice variants: understanding their multiple roles in health and
723 disease using engineered mouse models. *IUBMB Life* **63**, 538-546 (2011).
724 10. Lin TC, et al., Fibronectin in cancer: Friend or foe. *Cells* **9**, (2019).
725 11. Astrof S, Crowley D, Hynes RO, Multiple cardiovascular defects caused by the absence of
726 alternatively spliced segments of fibronectin. *Dev Biol* **311**, 11-24 (2007).
727 12. Dalton CJ, Lemmon CA, Fibronectin: Molecular structure, fibrillar structure and mechanochemical
728 signaling. *Cells* **10**, (2021).
729 13. George EL, Georges-Labouesse EN, Patel-King RS, Rayburn H, Hynes RO, Defects in mesoderm,
730 neural tube and vascular development in mouse embryos lacking fibronectin. *Development* **119**,
731 1079-1091 (1993).
732 14. Takahashi S, et al., The RGD motif in fibronectin is essential for development but dispensable for
733 fibril assembly. *J Cell Biol* **178**, 167-178 (2007).
734 15. Castelletti F, et al., Mutations in FN1 cause glomerulopathy with fibronectin deposits. *Proc Natl*
735 *Acad Sci USA* **105**, 2538-2543 (2008).
736 16. Lee CS, et al., Mutations in fibronectin cause a subtype of spondylometaphyseal dysplasia with
737 “corner fractures”. *Am J Hum Genet* **101**, 815-823 (2017).
738 17. Costantini A, et al., Novel fibronectin mutations and expansion of the phenotype in
739 spondylometaphyseal dysplasia with "corner fractures". *Bone* **121**, 163-171 (2019).
740 18. Cadoff EB, et al., Mechanistic insights into the cellular effects of a novel FN1 variant associated with
741 a spondylometaphyseal dysplasia. *Clin Genet* **94**, 429-437 (2018).
742 19. Newman B, Wallis GA, Skeletal dysplasias caused by a disruption of skeletal patterning and
743 endochondral ossification. *Clin Genet* **63**, 241-251 (2003).
744 20. Tsang KY, Tsang SW, Chan D, Cheah KS, The chondrocytic journey in endochondral bone growth and
745 skeletal dysplasia. *Birth Defects Res* **102**, 52-73 (2014).
746 21. Kulyk WM, Upholt WB, Kosher RA, Fibronectin gene expression during limb cartilage differentiation.
747 *Development* **106**, 449-455 (1989).
748 22. Singh P, Schwarzbauer JE, Fibronectin matrix assembly is essential for cell condensation during
749 chondrogenesis. *J Cell Sci* **127**, 4420-4428 (2014).
750 23. Rein S, et al., Immunofluorescence analysis of sensory nerve endings in the interosseous membrane
751 of the forearm. *J Anat* **236**, 906-915 (2020).
752 24. Nag R, Paul RR, Pal M, Chatterjee J, Das RK, Epithelial distribution of E-cadherin, p63, and mitotic
753 figures in ApoTome images to determine the oncogenic potentiality of oral submucous fibrosis.
754 *Microscopy and Microanalysis* **26**, 1198-1210 (2020).

755 25. Hendershot LM, The ER function BiP is a master regulator of ER function. *Mt Sinai J Med* **71**, 289-297
756 (2004).
757 26. Haas IG, BiP (GRP78), an essential hsp70 resident protein in the endoplasmic reticulum. *Experientia*
758 **50**, 1012-1020 (1994).
759 27. Ito S, Nagata K, Roles of the endoplasmic reticulum-resident, collagen-specific molecular chaperone
760 Hsp47 in vertebrate cells and human disease. *J Biol Chem* **294**, 2133-2141 (2019).
761 28. Kang J, et al., Ribosomal proteins and human diseases: molecular mechanisms and targeted
762 therapy. *Signal Transduct Target Ther* **6**, 323 (2021).
763 29. Bucci C, et al., The small GTPase rab5 functions as a regulatory factor in the early endocytic
764 pathway. *Cell* **70**, 715-728 (1992).
765 30. Vanlandingham PA, Ceresa BP, Rab7 regulates late endocytic trafficking downstream of
766 multivesicular body biogenesis and cargo sequestration. *J Biol Chem* **284**, 12110-12124 (2009).
767 31. Peng J, et al., Atg5 regulates late endosome and lysosome biogenesis. *Sci China Life Sci* **57**, 59-68
768 (2014).
769 32. Liang T, et al., Identifying the key genes regulating mesenchymal stem cells chondrogenic
770 differentiation: an in vitro study. *BMC Musculoskelet Disord* **23**, 985 (2022).
771 33. Qiu XB, Shao YM, Miao S, Wang L, The diversity of the DnaJ/Hsp40 family, the crucial partners for
772 Hsp70 chaperones. *Cell Mol Life Sci* **63**, 2560-2570 (2006).
773 34. Forster ML, et al., Protein disulfide isomerase-like proteins play opposing roles during
774 retrotranslocation. *J Cell Biol* **173**, 853-859 (2006).
775 35. Gillece P, Luz JM, Lennarz WJ, de La Cruz FJ, Romisch K, Export of a cysteine-free misfolded
776 secretory protein from the endoplasmic reticulum for degradation requires interaction with protein
777 disulfide isomerase. *J Cell Biol* **147**, 1443-1456 (1999).
778 36. Wek RC, Role of eIF2alpha kinases in translational control and adaptation to cellular stress. *Cold*
779 *Spring Harb Perspect Biol* **10**, (2018).
780 37. Ninagawa S, et al., EDEM2 initiates mammalian glycoprotein ERAD by catalyzing the first mannose
781 trimming step. *J Cell Biol* **206**, 347-356 (2014).
782 38. Ghenea S, Chiritoiu M, Tacutu R, Miranda-Vizuete A, Petrescu SM, Targeting EDEM protects against
783 ER stress and improves development and survival in C. elegans. *PLoS Genet* **18**, e1010069 (2022).
784 39. Pankov R, Yamada KM, Fibronectin at a glance. *J Cell Sci* **115**, 3861-3863 (2002).
785 40. Akiyama SK, Yamada SS, Chen WT, Yamada KM, Analysis of fibronectin receptor function with
786 monoclonal antibodies: roles in cell adhesion, migration, matrix assembly, and cytoskeletal
787 organization. *J Cell Biol* **109**, 863-875 (1989).
788 41. Fogerty FJ, Akiyama SK, Yamada KM, Mosher DF, Inhibition of binding of fibronectin to matrix
789 assembly sites by anti-integrin (alpha 5 beta 1) antibodies. *J Cell Biol* **111**, 699-708 (1990).
790 42. Wu C, Keivens VM, O'Toole TE, McDonald JA, Ginsberg MH, Integrin activation and cytoskeletal
791 interaction are essential for the assembly of a fibronectin matrix. *Cell* **83**, 715-724 (1995).
792 43. Kornmann B, et al., An ER-mitochondria tethering complex revealed by a synthetic biology screen.
793 *Science* **325**, 477-481 (2009).
794 44. Vance JE, Phospholipid synthesis in a membrane fraction associated with mitochondria. *J Biol Chem*
795 **265**, 7248-7256 (1990).
796 45. Bravo R, et al., Endoplasmic reticulum: ER stress regulates mitochondrial bioenergetics. *Int J*
797 *Biochem Cell Biol* **44**, 16-20 (2012).
798 46. Long F, Ornitz DM, Development of the endochondral skeleton. *Cold Spring Harb Perspect Biol* **5**,
799 (2013).
800 47. Greco KV, et al., High density micromass cultures of a human chondrocyte cell line: a reliable assay
801 system to reveal the modulatory functions of pharmacological agents. *Biochem Pharmacol* **82**, 1919-
802 1929 (2011).
803 48. Ryu NE, Lee SH, Park H, Spheroid culture system methods and applications for mesenchymal stem
804 cells. *Cells* **8**, (2019).

805 49. Rolfe RA, Shea CA, Murphy P, Geometric analysis of chondrogenic self-organisation of embryonic
806 limb bud cells in micromass culture. *Cell Tissue Res* **388**, 49-62 (2022).
807 50. Lu TJ, Chiu FY, Chiu HY, Chang MC, Hung SC, Chondrogenic Differentiation of Mesenchymal Stem
808 Cells in Three-Dimensional Chitosan Film Culture. *Cell Transplant* **26**, 417-427 (2017).
809 51. Xu Y, et al., Analysis of the material properties of early chondrogenic differentiated adipose-derived
810 stromal cells (ASC) using an in vitro three-dimensional micromass culture system. *Biochem Biophys*
811 *Res Commun* **359**, 311-316 (2007).
812 52. Tang Y, et al., A comparative assessment of adipose-derived stem cells from subcutaneous and
813 visceral fat as a potential cell source for knee osteoarthritis treatment. *J Cell Mol Med* **21**, 2153-
814 2162 (2017).
815 53. Lamande SR, et al., Modeling human skeletal development using human pluripotent stem cells. *Proc*
816 *Natl Acad Sci USA* **120**, e2211510120 (2023).
817 54. van Hoolwerff M, et al., Identification and functional characterization of imbalanced osteoarthritis-
818 associated fibronectin splice variants. *Rheumatology* **62**, 894-904 (2023).
819 55. Wang W, Rigueur D, Lyons KM, TGFbeta signaling in cartilage development and maintenance. *Birth*
820 *Defects Res* **102**, 37-51 (2014).
821 56. Williams MJ, et al., Solution structure of a pair of fibronectin type 1 modules with fibrin binding
822 activity. *J Mol Biol* **235**, 1302-1311 (1994).
823 57. Oberhauser AF, Badilla-Fernandez C, Carrion-Vazquez M, Fernandez JM, The mechanical hierarchies
824 of fibronectin observed with single-molecule AFM. *J Mol Biol* **319**, 433-447 (2002).
825 58. Sottile J, Schwarzbauer J, Selegue J, Mosher DF, Five type I modules of fibronectin form a functional
826 unit that binds to fibroblasts and Staphylococcus aureus. *J Biol Chem* **266**, 12840-12843 (1991).
827 59. Kamimoto T, et al., Intracellular inclusions containing mutant alpha1-antitrypsin Z are propagated in
828 the absence of autophagic activity. *J Biol Chem* **281**, 4467-4476 (2006).
829 60. Fregno I, et al., ER-to-lysosome-associated degradation of proteasome-resistant ATZ polymers
830 occurs via receptor-mediated vesicular transport. *EMBO J* **37**, (2018).
831 61. Fregno I, Fasana E, Solda T, Galli C, Molinari M, N-glycan processing selects ERAD-resistant
832 misfolded proteins for ER-to-lysosome-associated degradation. *EMBO J* **40**, e107240 (2021).
833 62. Noda T, Farquhar MG, A non-autophagic pathway for diversion of ER secretory proteins to
834 lysosomes. *J Cell Biol* **119**, 85-97 (1992).
835 63. Jin H, Komita M, Aoe T, The role of BiP retrieval by the KDEL receptor in the early secretory pathway
836 and its effect on protein quality control and neurodegeneration. *Front Mol Neurosci* **10**, 222 (2017).
837 64. Yin L, Zhou Y, Liu H, Li Y, LYECs: lysosome-enhancing compounds as potential therapeutic
838 approaches for Alzheimer disease. *Autophagy* **19**, 1863-1864 (2023).
839 65. Czaja MJ, et al., Functions of autophagy in normal and diseased liver. *Autophagy* **9**, 1131-1158
840 (2013).
841 66. Coelho CN, Kosher RA, Gap junctional communication during limb cartilage differentiation. *Dev Biol*
842 **144**, 47-53 (1991).
843 67. Hall BK, Miyake T, All for one and one for all: condensations and the initiation of skeletal
844 development. *Bioessays* **22**, 138-147 (2000).
845 68. Goldring MB, Tsuchimochi K, Ijiri K, The control of chondrogenesis. *J Cell Biochem* **97**, 33-44 (2006).
846 69. Dexheimer V, Frank S, Richter W, Proliferation as a requirement for in vitro chondrogenesis of
847 human mesenchymal stem cells. *Stem Cells Dev* **21**, 2160-2169 (2012).
848 70. Nishioka T, et al., ATX-LPA1 axis contributes to proliferation of chondrocytes by regulating
849 fibronectin assembly leading to proper cartilage formation. *Sci Rep* **6**, 23433 (2016).
850 71. van Hoolwerff M, et al., High-impact FN1 mutation decreases chondrogenic potential and affects
851 cartilage deposition via decreased binding to collagen type II. *Sci Adv* **7**, eabg8583 (2021).
852 72. McHugh KP, et al., Mice lacking beta3 integrins are osteosclerotic because of dysfunctional
853 osteoclasts. *J Clin Invest* **105**, 433-440 (2000).
854 73. R. D, H. H, J. B, Role of syndecan-4 in chondrocyte differentiation. *Ann Rheum Dis* **70**, 90-91 (2011).

855 74. Matsunobu T, et al., Critical roles of the TGF-beta type I receptor ALK5 in perichondrial formation
856 and function, cartilage integrity, and osteoblast differentiation during growth plate development.
857 *Dev Biol* **332**, 325-338 (2009).
858 75. Longobardi L, et al., TGF-beta type II receptor/MCP-5 axis: at the crossroad between joint and
859 growth plate development. *Dev Cell* **23**, 71-81 (2012).
860 76. Zhang H, et al., FN1 promotes chondrocyte differentiation and collagen production via TGF-
861 beta/PI3K/Akt pathway in mice with femoral fracture. *Gene* **769**, 145-253 (2021).
862 77. Benabdallah B, et al., Myogenic progenitor cells derived from human induced pluripotent stem cell
863 are immune-tolerated in humanized mice. *Stem Cells Transl Med* **10**, 267-277 (2021).
864 78. Schneider CA, Rasband WS, Eliceiri KW, NIH Image to ImageJ: 25 years of image analysis. *Nat*
865 *Methods* **9**, 671-675 (2012).
866 79. Bourgey M, et al., GenPipes: an open-source framework for distributed and scalable genomic
867 analyses. *GigaScience* **8**, (2019).
868 80. Bolger AM, Lohse M, Usadel B, Trimmomatic: a flexible trimmer for Illumina sequence data.
869 *Bioinformatics* **30**, 2114-2120 (2014).
870 81. Dobin A, et al., STAR: ultrafast universal RNA-seq aligner. *Bioinformatics* **29**, 15-21 (2013).
871 82. Anders S, Pyl PT, Huber W, HTSeq--a Python framework to work with high-throughput sequencing
872 data. *Bioinformatics* **31**, 166-169 (2015).
873 83. Love MI, Huber W, Anders S, Moderated estimation of fold change and dispersion for RNA-seq data
874 with DESeq2. *Genome Biol* **15**, 550 (2014).
875 84. Stephens M, False discovery rates: a new deal. *Biostatistics* **18**, 275-294 (2017).
876 85. Mirdita M, et al., ColabFold: making protein folding accessible to all. *Nat Methods* **19**, 679-682
877 (2022).
878 86. Barber RD, Software to visualize proteins and perform structural alignments. *Curr Protoc* **1**, e292
879 (2021).
880 87. Rosignoli S, Paiardini A, Boosting the full potential of PyMOL with structural biology plugins.
881 *Biomolecules* **12**, (2022).
882 88. Zhang RM, Kumra H, Reinhardt DP, Quantification of extracellular matrix fiber systems related to
883 ADAMTS proteins. *Methods Mol Biol* **2043**, 237-250 (2019).

884 # Figure Legends

885

886 **Figure 1. Generation of an SMDCF cell model system.**

887 **(A)** Schematic overview of an SMDCF model system using iPSCs with SMDCF causing FN mutations. IPSCs were
888 cultured and differentiated into MSCs and then into chondrocytes. The two FN mutations analyzed in this
889 study are p.Cys123Arg affecting the FNI-2 domain and p.Cys231Trp affecting the FNI-5 domain. **(B)** IPSCs were
890 evaluated by flow cytometry for the expression of pluripotent stem cell markers with specific antibodies
891 against SOX2, NANOG, C-MYC and OCT4. Positive control cell populations are represented in blue, FN_{C123R}
892 mutants in red and FN_{C231W} mutants in green. Fluorescence minus one (FMO, grey) for each of the antibody
893 was used as the negative control per cell group. **(C)** Sequencing of *FN1* mRNA from iPSC-derived MSCs after
894 amplification by PCR, confirming the heterozygous FN mutations as indicated by arrows. **(D)** Analysis of iPSC-
895 derived MSCs for the expression of MSC markers CD73, CD105 and undifferentiated marker TRA-1-60. Positive
896 control cell populations are represented in blue, FN_{C123R} mutants in green, and FN_{C231W} mutants in red.
897 Fluorescence minus one (FMO, cyan) for each of the antibodies was used as the negative control per cell
898 group.

899

900 **Figure 2. SMDCF mutations in FN cause cellular and matrix defects.**

901 **(A)** *In silico* structure prediction and comparison of the wild type and FN mutant domains (FNI-2, FNI-3, FNI-
902 4, FNI-5) using AlphaFold 2.0 and PyMOL. **(B)** Immunostaining images for FN in an unaffected control and the
903 FN mutant MSCs (FN in green, top panel) and in chondrocyte micromasses (FN in red, bottom panel) using
904 an anti-fibronectin antibody. Figure shows representative images from three independent experiments (n=3).
905 Matrix
906 staining for FN is denoted by black arrow and intracellular staining by white arrows. Nuclear counterstaining
907 using DAPI is represented in blue. Relative to MSCs in monolayers, cells in micromasses show a significantly
908 smaller cell size. **(C)** Relative gene expression of *FN1* in control and mutant MSCs. Each data point in the graph
909 represents the average of technical triplicates or duplicates from 6 different samples per cell group (n=6).
910 Error bar represents ± SEM. Statistical analysis was performed using one-way ANOVA with Bonferroni post-
911 test. **(D-F)** Protein lysates and condition media from control and mutant MSC cultures immunoblotted for FN
912 (~220-250 kDa) under reducing conditions. GAPDH (37kDa) was used as the internal loading control. **(E-F)**
913 Quantification of representative immunoblots shown in **(D)** from three independent experiments (n=3). **(G)**
914 Immunoblotting for FN using serum samples obtained from an unaffected individual (*Control*) and the SMDCF
915 patients with the FN_{C123R} and FN_{C231W} mutations. Note the bottom panel represents loading control of pierce
916 blue staining for total protein level **(H-I)** Immunostaining of proliferation marker Ki-67 (green) using control
917 and mutant MSCs. Ki-67 positive cells were quantified and normalized to the total cell count. Each data point
918 represents the average percentage of Ki-67 positive cells from individual images of one representative
919 experiment of total 4 independent experiments. Error bar represents ± SD. Statistical analysis was performed
920 using one-way ANOVA with Bonferroni post-test. **(J)** Side scatter (SSC-A) versus forward scatter (FSC-H) plot
921 obtained from flow cytometry experiments using control and FN mutant MSCs. The control cell population is
922 represented in blue, FN_{C123R} mutant in green, and FN_{C231W} mutant in red.

923

924 **Figure 3. Transmission electron microscopy show massive accumulation of vesicular structures in**
925 **the SMDCF MSCs.**

926 **(A, I-III)** Control cells show normal nucleus (N), Golgi apparatus (G), rough endoplasmic reticulum (R),
927 ribosomes (RB), and mitochondria (M) (arrowheads). **(B,C, I-III)** Patient MSCs show accumulation of dense
928 vesicular structures (VS) frequently covered with ribosomes (arrowheads). **(B, C, III)** Arrowheads indicate
929 vesicles bulging out from the rough ER in both FN_{C123R} and FN_{C231W} MSCs. Magnifications are 1200× in I, 6800×

930 in II, and 30,000× in III. **(D-E)** Histogram of mutant protein-containing vesicle area (bin size = 1 μm^2 in **D** and 5
931 μm^2 in **E**). 100% represents the total area of all analyzed vesicles. The average vesicle area was 0.52 μm^2 in
932 FN_{C123R} and 1.49 μm^2 in FN_{C231W}. More than 700 vesicles were quantified per mutant group in a total of 10-12
933 cells.
934

935 **Figure 4. FN immunogold labelling of control and mutant MSCs.**

936 **(A-C)** Immunogold labelling of control and mutant MSCs was performed using an anti-FN antibody (αhFN) and
937 12nm gold conjugated secondary antibodies. **(A)** Control cells primarily showed gold particles on FN positive
938 fibers outside the cells (arrowheads). **(B-C)** FN mutant MSCs showed intensive gold labeling in all dense
939 vesicular structures, confirming that the mutant FN accumulated in these vesicles (arrowheads). **(A- C)** The
940 no αhFN controls for each cell group did not display any gold labels. Scale bars are indicated in each image.
941

942 **Figure 5. Indirect immunofluorescence analyses of subcellular compartment markers show that**
943 **mutant FN is transported directly from the RER to lysosomes.**

944 Double immunostaining of control and mutant MSCs was performed with antibodies against FN (green) and
945 against marker proteins for various subcellular compartments (red). Nuclear counter stain by DAPI appears in
946 blue. Single channels are shown in grayscale, and overlaid images are pseudocolored as indicated. Markers
947 included the chaperones BIP **(A,B,** Insets show ~2-fold magnified vesicle**)** and HSP47 **(C,D)** the ribosomal
948 marker RSP6 **(E)**, the early endosomal marker RAB5, late endosomal marker RAB7, autophagy marker LC3,
949 and Golgi apparatus marker GM103 **(F)**, and the lysosomal markers LAMP1 **(G,H)** and ATG5 **(I)**. Figures display
950 representative images of a total of three independent experiments (n=3). Each data point in the quantification
951 graphs represents an individual cell, n = 41–121 cells per group and error bars represent ± SD. Statistics was
952 assessed by unpaired Student's two tailed t-test. Scale bar represents 20µm for all images.
953

954 **Figure 6. RNA sequencing analysis of protein folding chaperones and ribosomal markers.**

955 Control and mutant cells were analyzed by bulk RNA sequencing at the MSC and differentiated chondrocyte
956 stage. **(A-C)** Heat maps of the differential gene expression for protein folding chaperones in the HSP40 group.
957 **(D-F)** Heat maps of gene expression categorized into the large and small ribosomal marker groups. For all heat
958 maps, the rlog counts determined from 3 technical replicates per each sample group are shown color coded.
959 The colors for the lowest and highest rlog values are indicated on the right. Statistical analysis was performed
960 using nbinomWaldTest followed by the Benjamini-Hochberg method. For each group, genes with significance
961 of $p \leq 0.05$ are shown in ascending order with the lowest p-values on top. FC (log2) represents the log2 of the
962 fold change comparing control chondrocytes to control MSCs **(A, D)**, and mutant chondrocytes to control
963 chondrocytes **(B, C, E, F).**
964

965 **Figure 7. FN SMDCF mutants display increased ER stress markers and reduced expression of FN cell**
966 **receptors.**

967 Control and mutant SMDCF cells were analyzed by bulk RNA sequencing at the MSC and differentiated
968 chondrocyte stage. **(A)** Analysis of specific ER stress markers in control (red), FNC123R (blue), and FNC231W
969 (yellow) MSCs (top panel) and chondrocytes (bottom panel). **(B,C)** Heat maps of the mRNA levels of cell
970 surface receptors for FN in chondrocytes **(B)** and in MSCs **(C)**. Gene expression is represented in rlog counts
971 in 3 technical replicates per sample group (for heat maps color code on the right). The R package DESeq2 was
972 used to identify differences in expression levels between the groups. Statistical analysis was performed using
973 nbinomWaldTest followed by the Benjamini-Hochberg method. For the heat maps, genes with significance of
974 $p \leq 0.05$ are shown in ascending order with the lowest p-values on top. FC (log2) represents the log2 of the
975 fold change comparing control chondrocytes to control MSCs **(B**, left panel**)**, mutant chondrocytes to control
976 chondrocytes **(B,** middle and right panels**)**, and mutant MSCs to control MSCs **(C)**.

977 **Figure 8. FN mutants exhibit impaired mesenchymal stem cell condensation and differentiation**
978 **into chondrocytes.**

979 **(A)** Representative images of cell condensation assays. Images of condensing MSCs in control and FN mutants
980 from 6 h post cell seeding to 6 d. Scale bar represents 200 µm. **(B)** Quantification of micromass areas from
981 images taken at 6 d for control, FN_{C123R} and FNC231W samples. The graph represents data from three
982 independent experiments with a total n= 18-24 micromasses per sample group. Data are shown as means ±
983 SEM. Statistical analysis was performed with the unpaired Student's two tailed t-test. **(C)** Representative
984 images of double immunostaining of FN (green) and collagen type II (red) in control and mutant differentiated
985 micromass sections after 21 d chondrogenic differentiation. DAPI (blue) is used as a nuclear counterstain in
986 all images. Scale bar represents 20 µm for all images. **(D)** Quantification of the mean fluorescence intensity
987 of collagen type II from one representative experiment of a total of 3 independent experiments. Error bar
988 represents ± SD. Statistical analysis was performed using one-way ANOVA with Bonferroni post-test. **(E)**
989 *COL2A1* mRNA levels obtained from the RNAseq data in differentiated control and mutant cells (n=3).
990 Statistical analysis was performed using nbinomWaldTest followed.
991 by the Benjamin-Hochberg method.
992
993 **Figure 9. FN mutants exhibit reduced mRNA levels of chondrogenic markers.**

994 Control and mutant FN cells were analyzed by bulk RNA sequencing at the differentiated chondrocyte stage.
995 Graphs represent selected key chondrogenic markers expressed in FN mutant cells versus control
996 chondrocytes. Transcript reads for each marker is represented in rlog counts and sorted into two groups: **(A)**
997 matrix markers and **(B)** transcription factors, cell surface markers and growth factors. Data points represent
998 3 technical replicates per sample group. Statistical analysis was performed using nbinomWaldTest followed
999 by the Benjamini-Hochberg method. $P \leq 0.05$ was taken as significant for all analyzed data.
1000
1001 **Figure 10. Exogenous supplementation of FN and TGFβ1 can rescue condensation defect in FN**
1002 **mutant cells.**

1003 **(A,B)** Heat map of RNAseq data for markers in the TGFβ and BMP signaling pathways comparing **(A)** control
1004 MSCs and control chondrocytes, and **(B)** control and FN mutant chondrocytes. The rlog counts were
1005 determined from 3 technical replicates per sample and group. Statistical analysis was performed using
1006 nbinomWaldTest followed by the Benjamini-Hochberg method. For each group, only the mRNAs with
1007 significance of $p \leq 0.05$ are shown. FC (log2) represents the log2 of the fold change. **(C)** MSCs were analyzed
1008 for the presence of proliferation marker Ki-67 (green) using immunostaining under non-treated and FN (25
1009 µg/mL) or TGFβ1 (10 ng/mL) treated conditions. **(D)** Representative images of the live cell condensation assay
1010 of control versus FN mutant cells in non-treated (NT) and in FN or TGFβ1 treated conditions at 6 d. **(E)**
1011 Quantification of Ki-67 positive cells shown in (C) normalized to the total cell count. The graph represents Ki-
1012 67 positive cells from 12-17 images from three independent experiments (n=3). Each data point represents
1013 the average percentage of Ki-67 positive cells from one individual image. Error bar represents ± SEM.
1014 Significance was evaluated by the unpaired Student's two tailed t-test. **(F)** Quantification of micromass areas
1015 shown in (D). The graph represents data from five independent experiments with a total n=30-40
1016 micromasses per sample group. Data are shown as means ± SEM. Statistical analysis was performed with the
1017 unpaired Student's two tailed t-test.
1018
1019 **Figure 11. Schematic representation of the molecular mechanism and pathways proposed for**
1020 **SMDCF pathogenesis.**

1021 **(A)** Schematic overview of FN secretion and assembly of an unaffected cell and in mesenchymal condensation
1022 and chondrogenesis. **(B)** Overview of the proposed intracellular and extracellular mechanisms contributing to

1023 the pathogenesis of SMDCF in FN mutant stem cells. Details are described in the main text. Note the various
1024 components in the figure are not drawn to scale.

Figure 1

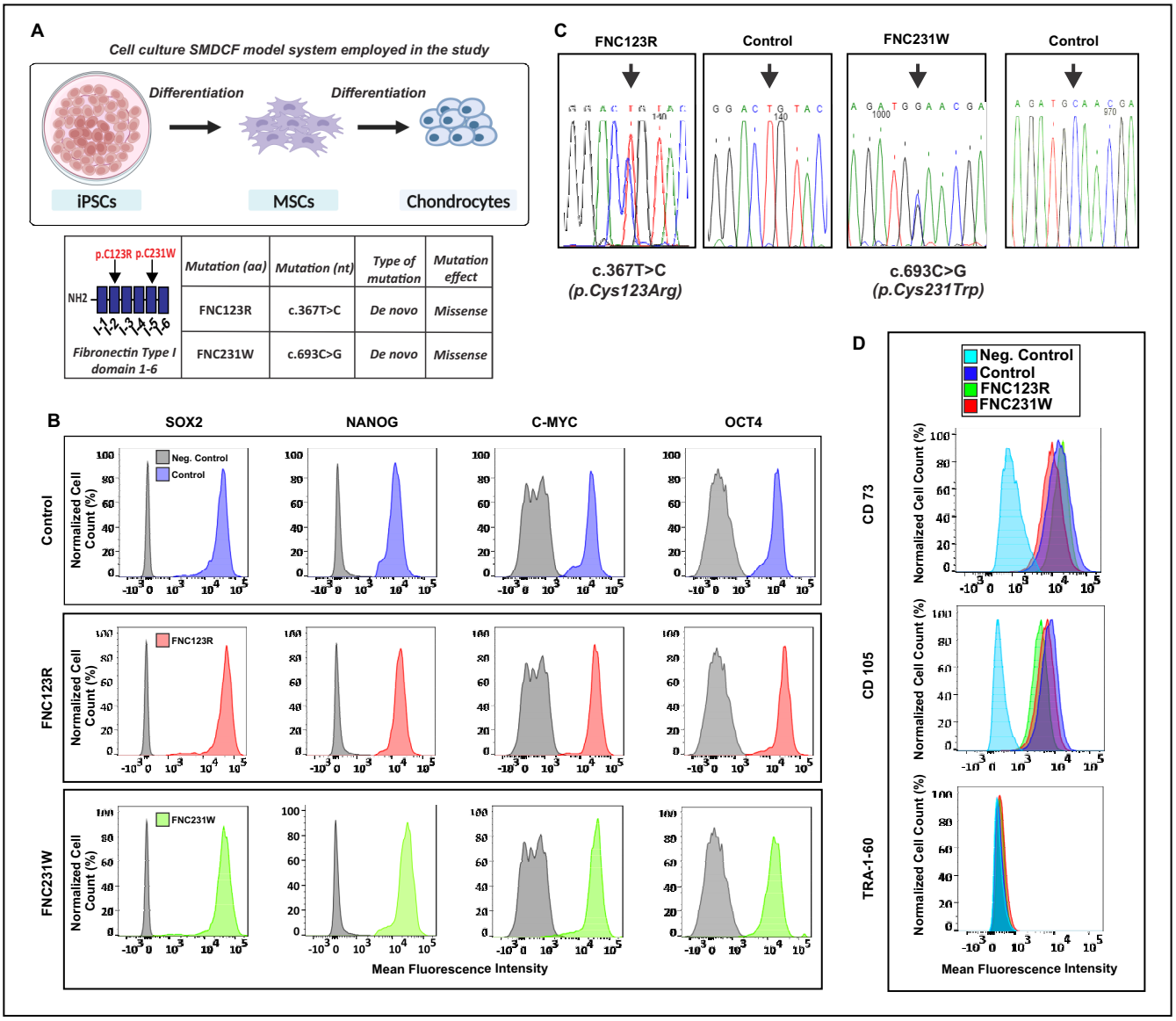
A
Cell culture SMDCF model system employed in the study
Differentiation
Differentiation
iPSCs
MSCs
Chondrocytes
p.C123R p.C231W
NH2
1-1 1-2 1-3 1-4 1-5 1-6
Fibronectin Type I domain 1-6
Mutation (aa)
Mutation (nt)
Type of mutation
Mutation effect
FNC123R
c.367T>C
De novo
Missense
FNC231W
c.693C>G
De novo
Missense
C
FNC123R
Control
FNC231W
Control
c.367T>C
(p.Cys123Arg)
c.693C>G
(p.Cys231Trp)
B
SOX2
NANOG
C-MYC
OCT4
Control
FNC123R
FNC231W
Neg. Control
Control
FNC123R
FNC231W
Normalized Cell Count (%)
Mean Fluorescence Intensity
D
Neg. Control
Control
FNC123R
FNC231W
CD 73
CD 105
TRA-1-60
Normalized Cell Count (%)
Mean Fluorescence Intensity

Figure 2

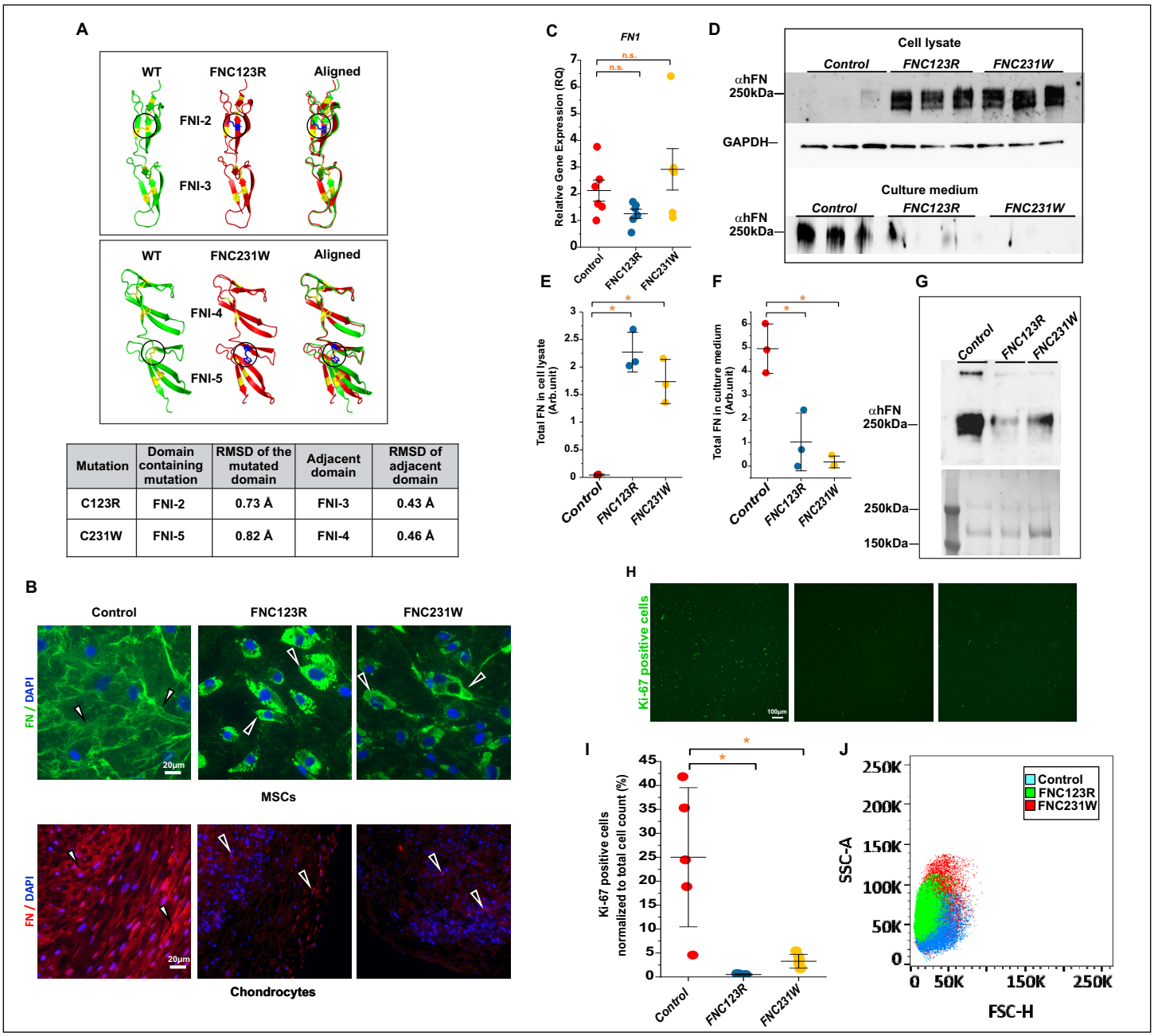

Mutation	Domain containing mutation	RMSD of the mutated domain	Adjacent domain	RMSD of adjacent domain
C123R	FNI-2	0.73 Å	FNI-3	0.43 Å
C231W	FNI-5	0.82 Å	FNI-4	0.46 Å

Figure 3

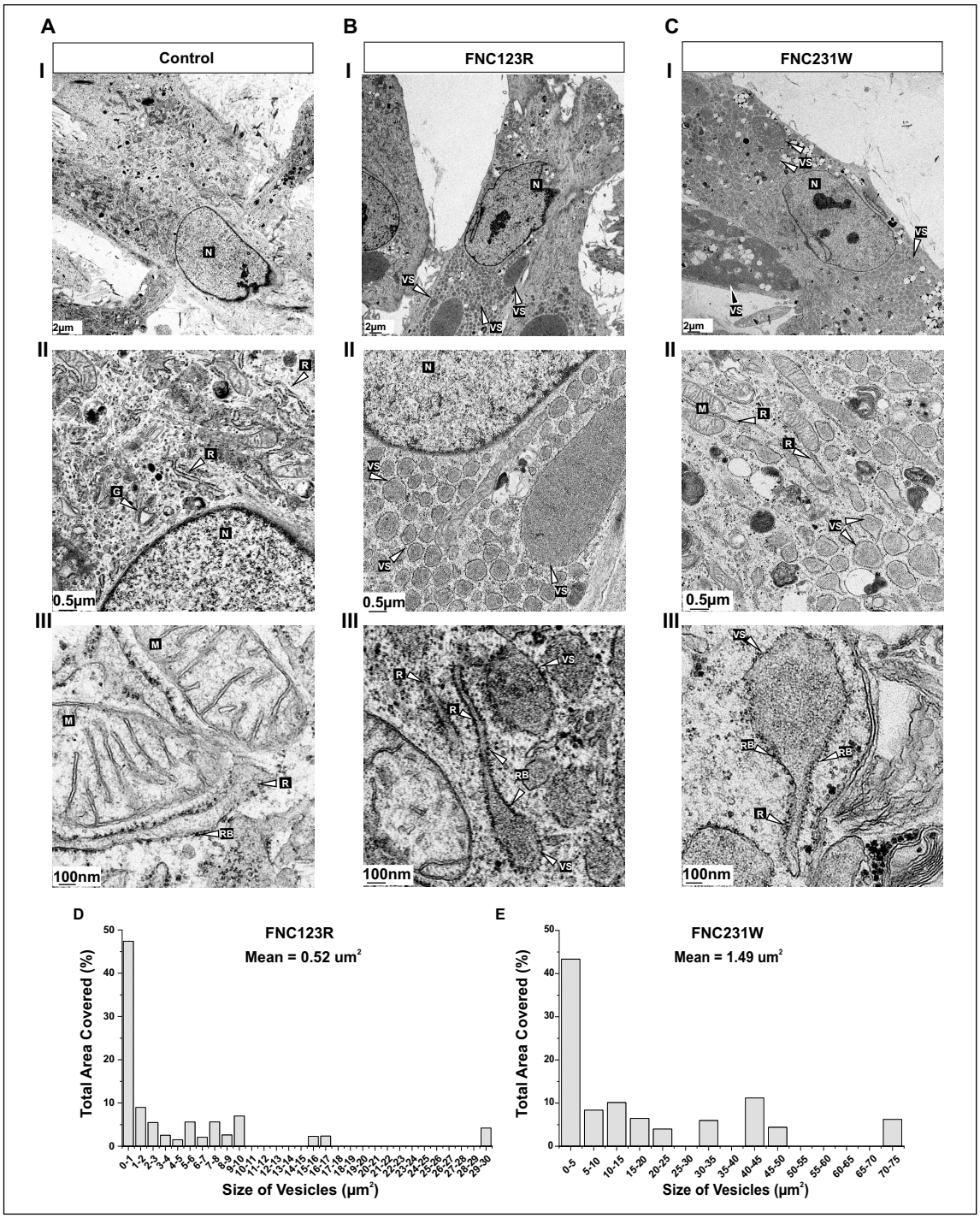
A
B
C
Control
FNC123R
FNC231W
I
II
III
N
VS
R
G
M
RB
2µm
0.5µm
100nm
D
E
FNC123R
Mean = 0.52 um²
FNC231W
Mean = 1.49 um²
Total Area Covered (%)
Size of Vesicles (µm²)

Figure 4

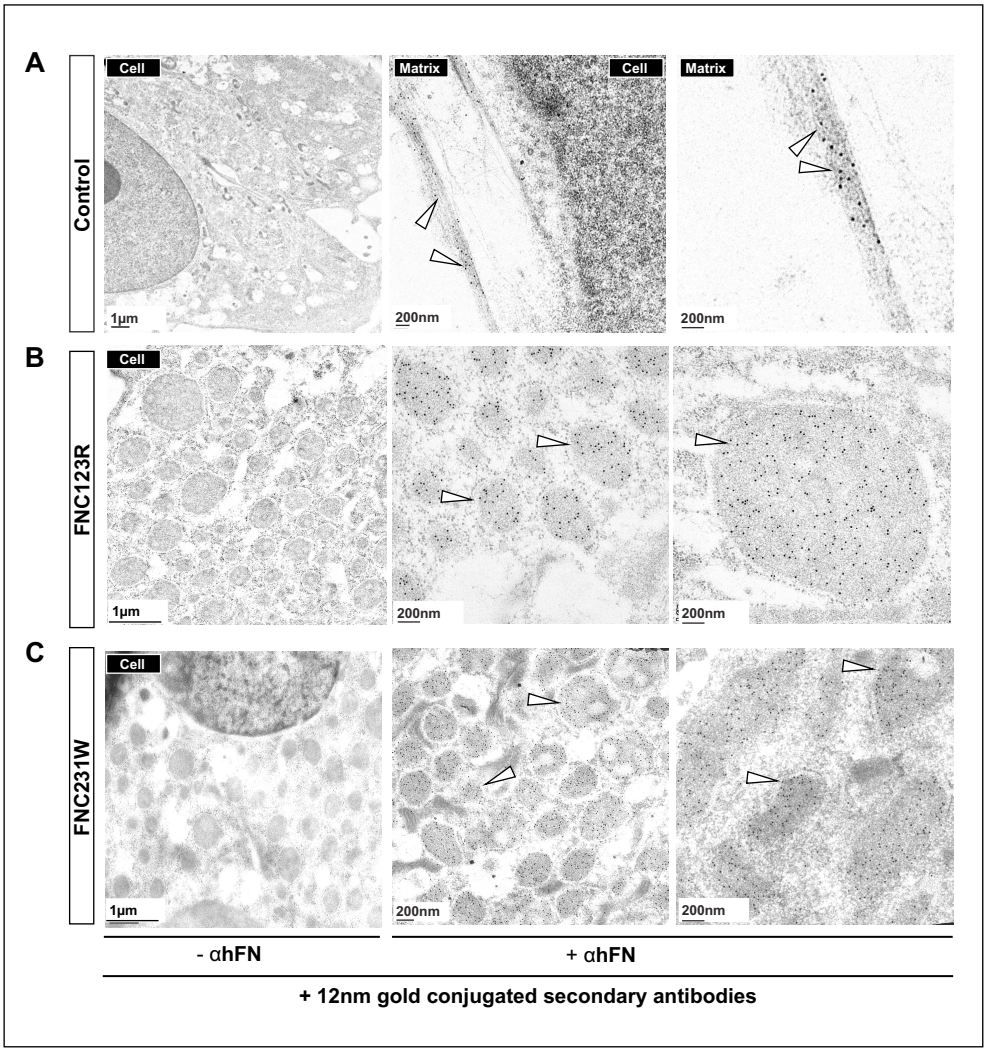
A
Control
Cell
Matrix
Cell
Matrix
1µm
200nm
200nm
B
FNC123R
Cell
1µm
200nm
200nm
C
FNC231W
Cell
1µm
200nm
200nm
- αhFN
+ αhFN
+ 12nm gold conjugated secondary antibodies

Figure 5

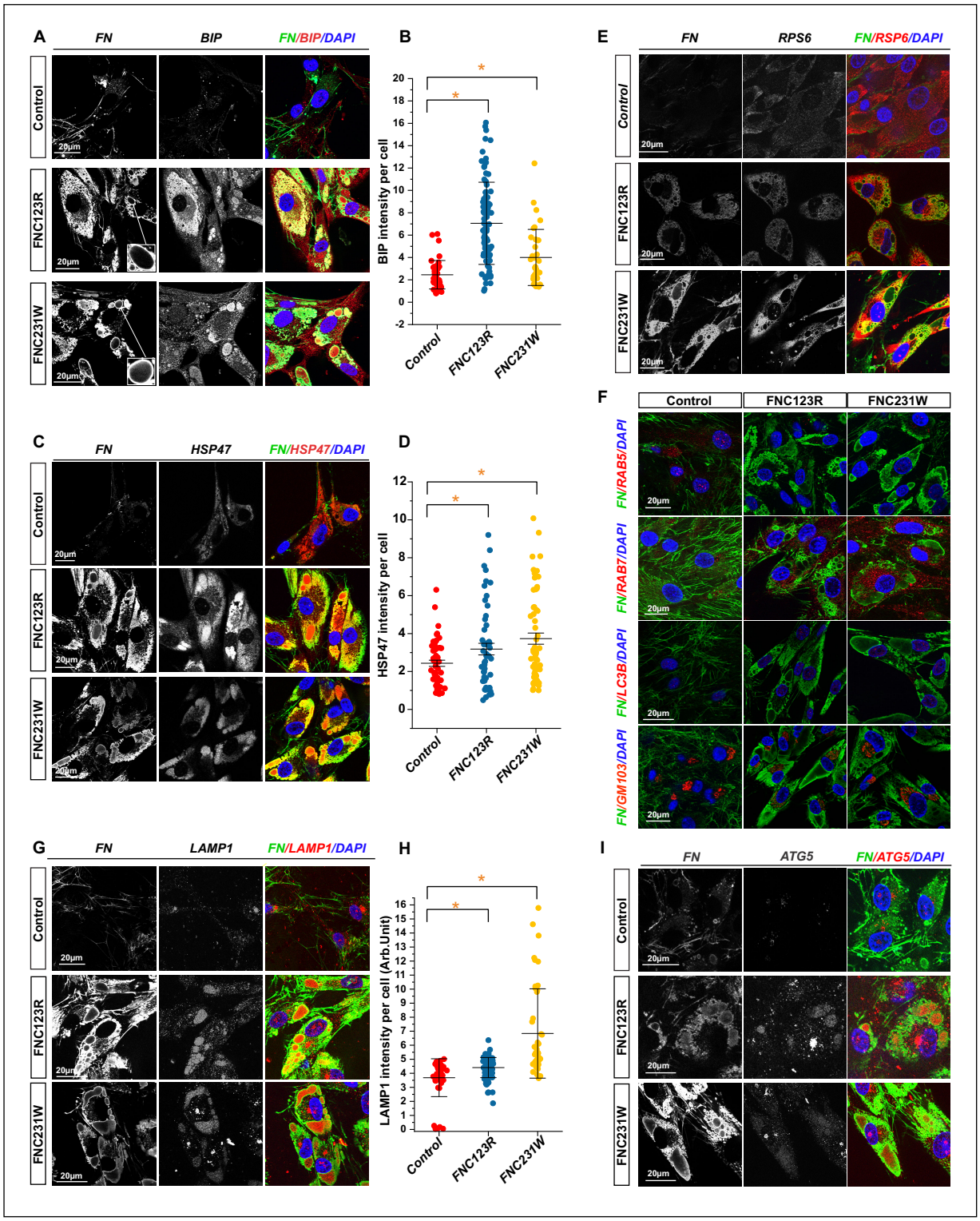
A
FN
BIP
FN/BIP/DAPI
Control
FNC123R
FNC231W
20μm
B
BIP intensity per cell
Control
FNC123R
FNC231W
C
FN
HSP47
FN/HSP47/DAPI
D
HSP47 intensity per cell
E
FN
RPS6
FN/RSP6/DAPI
F
Control
FNC123R
FNC231W
FN/RAB5/DAPI
FN/RAB7/DAPI
FN/LC3B/DAPI
FN/GM103/DAPI
G
FN
LAMP1
FN/LAMP1/DAPI
H
LAMP1 intensity per cell (Arb.Unit)
I
FN
ATG5
FN/ATG5/DAPI

Figure 6

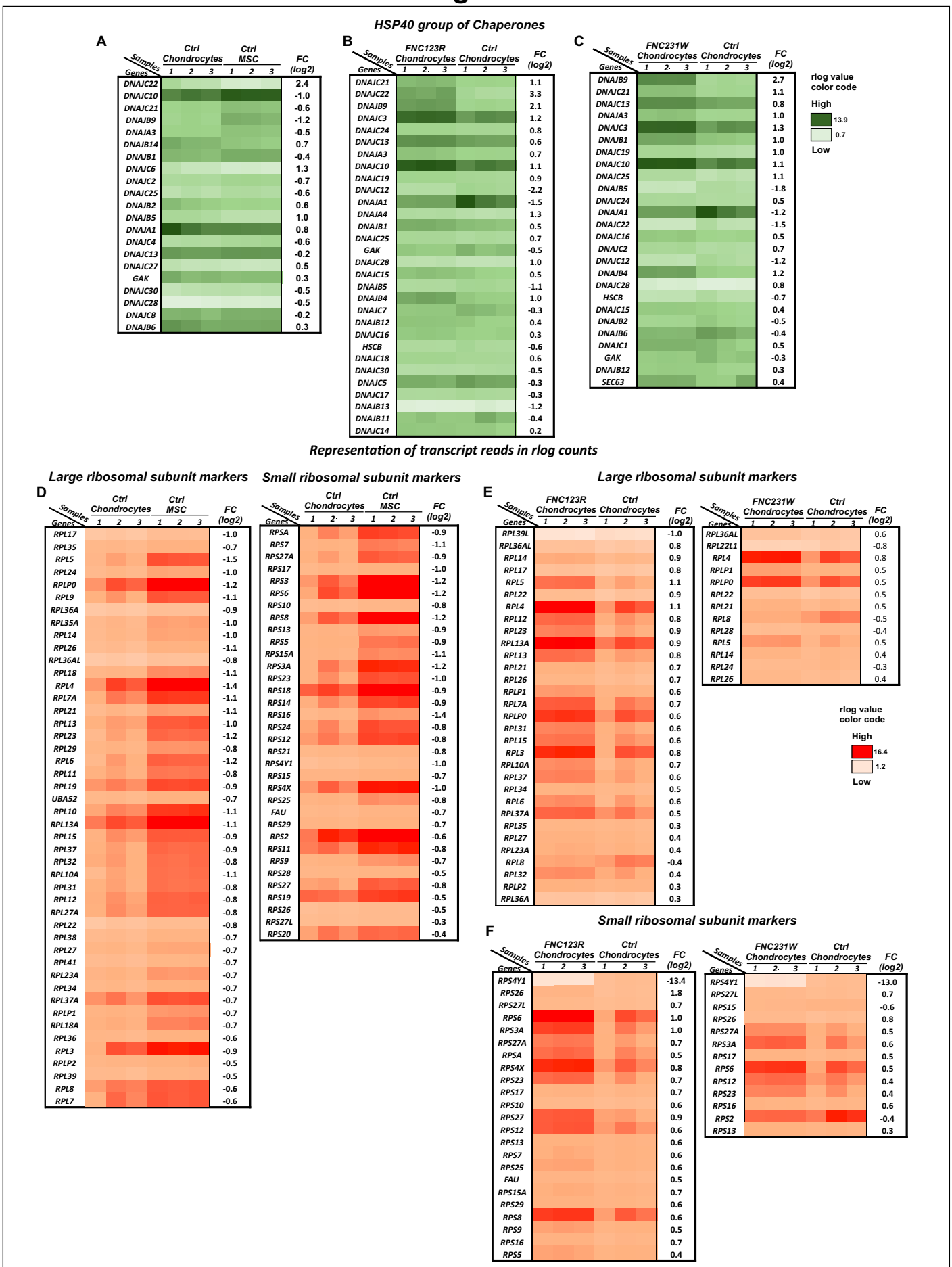
HSP40 group of Chaperones
A
Samples
Genes
Ctrl Chondrocytes
Ctrl MSC
1 2 3 1 2 3
FC (log2)
DNAJC22 2.4
DNAJC10 -1.0
DNAJC21 -0.6
DNAJB9 -1.2
DNAJA3 -0.5
DNAJB14 0.7
DNAJB1 -0.4
DNAJC6 1.3
DNAJC2 -0.7
DNAJC25 -0.6
DNAJB2 0.6
DNAJB5 1.0
DNAJA1 0.8
DNAJC4 -0.6
DNAJC13 -0.2
DNAJC27 0.5
GAK 0.3
DNAJC30 -0.5
DNAJC28 -0.5
DNAJC8 -0.2
DNAJB6 0.3
B
FNC123R Chondrocytes
Ctrl Chondrocytes
DNAJC21 1.1
DNAJC22 3.3
DNAJB9 2.1
DNAJC3 1.2
DNAJC24 0.8
DNAJC13 0.6
DNAJA3 0.7
DNAJC10 1.1
DNAJC19 0.9
DNAJC12 -2.2
DNAJA1 -1.5
DNAJA4 1.3
DNAJB1 0.5
DNAJC25 0.7
GAK -0.5
DNAJC28 1.0
DNAJC15 0.5
DNAJB5 -1.1
DNAJB4 1.0
DNAJC7 -0.3
DNAJB12 0.4
DNAJC16 0.3
HSCB -0.6
DNAJC18 0.6
DNAJC30 -0.5
DNAJC5 -0.3
DNAJC17 -0.3
DNAJB13 -1.2
DNAJB11 -0.4
DNAJC14 0.2
C
FNC231W Chondrocytes
Ctrl Chondrocytes
DNAJB9 2.7
DNAJC21 1.1
DNAJC13 0.8
DNAJA3 1.0
DNAJC3 1.3
DNAJB1 1.0
DNAJC19 1.0
DNAJC10 1.1
DNAJC25 1.1
DNAJB5 -1.8
DNAJC24 0.5
DNAJA1 -1.2
DNAJC22 -1.5
DNAJC16 0.5
DNAJC2 0.7
DNAJC12 -1.2
DNAJB4 1.2
DNAJC28 0.8
HSCB -0.7
DNAJC15 0.4
DNAJB2 -0.5
DNAJB6 -0.4
DNAJC1 0.5
GAK -0.3
DNAJB12 0.3
SEC63 0.4
rlog value color code
High
13.9
0.7
Low
Representation of transcript reads in rlog counts
Large ribosomal subunit markers
Small ribosomal subunit markers
D
Ctrl Chondrocytes
Ctrl MSC
RPL17 -1.0
RPL35 -0.7
RPL5 -1.5
RPL24 -1.0
RPLP0 -1.2
RPL9 -1.1
RPL36A -0.9
RPL35A -1.0
RPL14 -1.0
RPL26 -1.1
RPL36AL -0.8
RPL18 -1.1
RPL4 -1.4
RPL7A -1.1
RPL21 -1.1
RPL13 -1.0
RPL23 -1.2
RPL29 -0.8
RPL6 -1.2
RPL11 -0.8
RPL19 -0.9
UBA52 -0.7
RPL10 -1.1
RPL13A -1.1
RPL15 -0.9
RPL37 -0.9
RPL32 -0.8
RPL10A -1.1
RPL31 -0.8
RPL12 -0.8
RPL27A -0.8
RPL22 -0.8
RPL38 -0.7
RPL27 -0.7
RPL41 -0.7
RPL23A -0.7
RPL34 -0.7
RPL37A -0.7
RPLP1 -0.7
RPL18A -0.7
RPL36 -0.6
RPL3 -0.9
RPLP2 -0.5
RPL39 -0.5
RPL8 -0.6
RPL7 -0.6
RPSA -0.9
RPS7 -1.1
RPS27A -0.9
RPS17 -1.0
RPS3 -1.2
RPS6 -1.2
RPS10 -0.8
RPS8 -1.2
RPS13 -0.9
RPS5 -0.9
RPS15A -1.1
RPS3A -1.2
RPS23 -1.0
RPS18 -0.9
RPS14 -0.9
RPS16 -1.4
RPS24 -0.8
RPS12 -0.8
RPS21 -0.8
RPS4Y1 -1.0
RPS15 -0.7
RPS4X -1.0
RPS25 -0.8
FAU -0.7
RPS29 -0.7
RPS2 -0.6
RPS11 -0.8
RPS9 -0.7
RPS28 -0.5
RPS27 -0.8
RPS19 -0.5
RPS26 -0.5
RPS27L -0.3
RPS20 -0.4
E
FNC123R Chondrocytes
Ctrl Chondrocytes
RPL39L -1.0
RPL36AL 0.8
RPL14 0.9
RPL17 0.8
RPL5 1.1
RPL22 0.9
RPL4 1.1
RPL12 0.8
RPL23 0.9
RPL13A 0.9
RPL13 0.8
RPL21 0.7
RPL26 0.7
RPLP1 0.6
RPL7A 0.7
RPLP0 0.6
RPL31 0.6
RPL15 0.6
RPL3 0.8
RPL10A 0.7
RPL37 0.6
RPL34 0.5
RPL6 0.6
RPL37A 0.5
RPL35 0.3
RPL27 0.4
RPL23A 0.4
RPL8 -0.4
RPL32 0.4
RPLP2 0.3
RPL36A 0.3
FNC231W Chondrocytes
Ctrl Chondrocytes
RPL36AL 0.6
RPL22L1 -0.8
RPL4 0.8
RPLP1 0.5
RPLP0 0.5
RPL22 0.5
RPL21 0.5
RPL8 -0.5
RPL28 -0.4
RPL5 0.5
RPL14 0.4
RPL24 -0.3
RPL26 0.4
rlog value color code
High
16.4
1.2
Low
F
FNC123R Chondrocytes
Ctrl Chondrocytes
RPS4Y1 -13.4
RPS26 1.8
RPS27L 0.7
RPS6 1.0
RPS3A 1.0
RPS27A 0.7
RPSA 0.5
RPS4X 0.8
RPS23 0.7
RPS17 0.7
RPS10 0.6
RPS27 0.9
RPS12 0.6
RPS13 0.6
RPS7 0.6
RPS25 0.6
FAU 0.5
RPS15A 0.7
RPS29 0.6
RPS8 0.6
RPS9 0.5
RPS16 0.7
RPS5 0.4
FNC231W Chondrocytes
Ctrl Chondrocytes
RPS4Y1 -13.0
RPS27L 0.7
RPS15 -0.6
RPS26 0.8
RPS27A 0.5
RPS3A 0.6
RPS17 0.5
RPS6 0.5
RPS12 0.4
RPS23 0.4
RPS16 0.6
RPS2 -0.4
RPS13 0.3
Representation of transcript reads in rlog counts

Figure 7

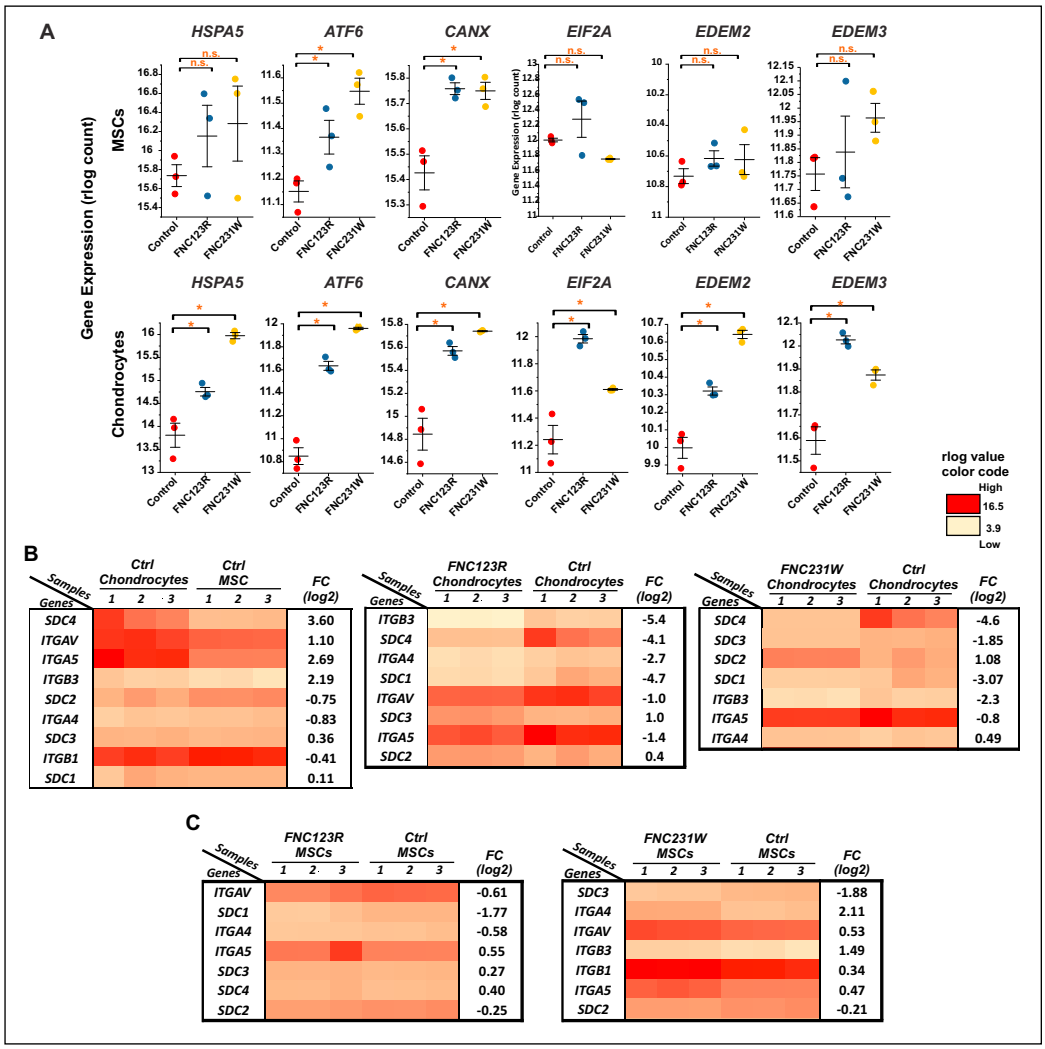
A
HSPA5
ATF6
CANX
EIF2A
EDEM2
EDEM3
MSCs
Chondrocytes
Gene Expression (rlog count)
n.s.
*
Control
FNC123R
FNC231W
rlog value color code
High
16.5
3.9
Low
B
Samples
Genes
Ctrl Chondrocytes
Ctrl MSC
FC (log2)
SDC4 3.60
ITGAV 1.10
ITGA5 2.69
ITGB3 2.19
SDC2 -0.75
ITGA4 -0.83
SDC3 0.36
ITGB1 -0.41
SDC1 0.11
FNC123R Chondrocytes
Ctrl Chondrocytes
ITGB3 -5.4
SDC4 -4.1
ITGA4 -2.7
SDC1 -4.7
ITGAV -1.0
SDC3 1.0
ITGA5 -1.4
SDC2 0.4
FNC231W Chondrocytes
Ctrl Chondrocytes
SDC4 -4.6
SDC3 -1.85
SDC2 1.08
SDC1 -3.07
ITGB3 -2.3
ITGA5 -0.8
ITGA4 0.49
C
FNC123R MSCs
Ctrl MSCs
ITGAV -0.61
SDC1 -1.77
ITGA4 -0.58
ITGA5 0.55
SDC3 0.27
SDC4 0.40
SDC2 -0.25
FNC231W MSCs
Ctrl MSCs
SDC3 -1.88
ITGA4 2.11
ITGAV 0.53
ITGB3 1.49
ITGB1 0.34
ITGA5 0.47
SDC2 -0.21

Figure 8

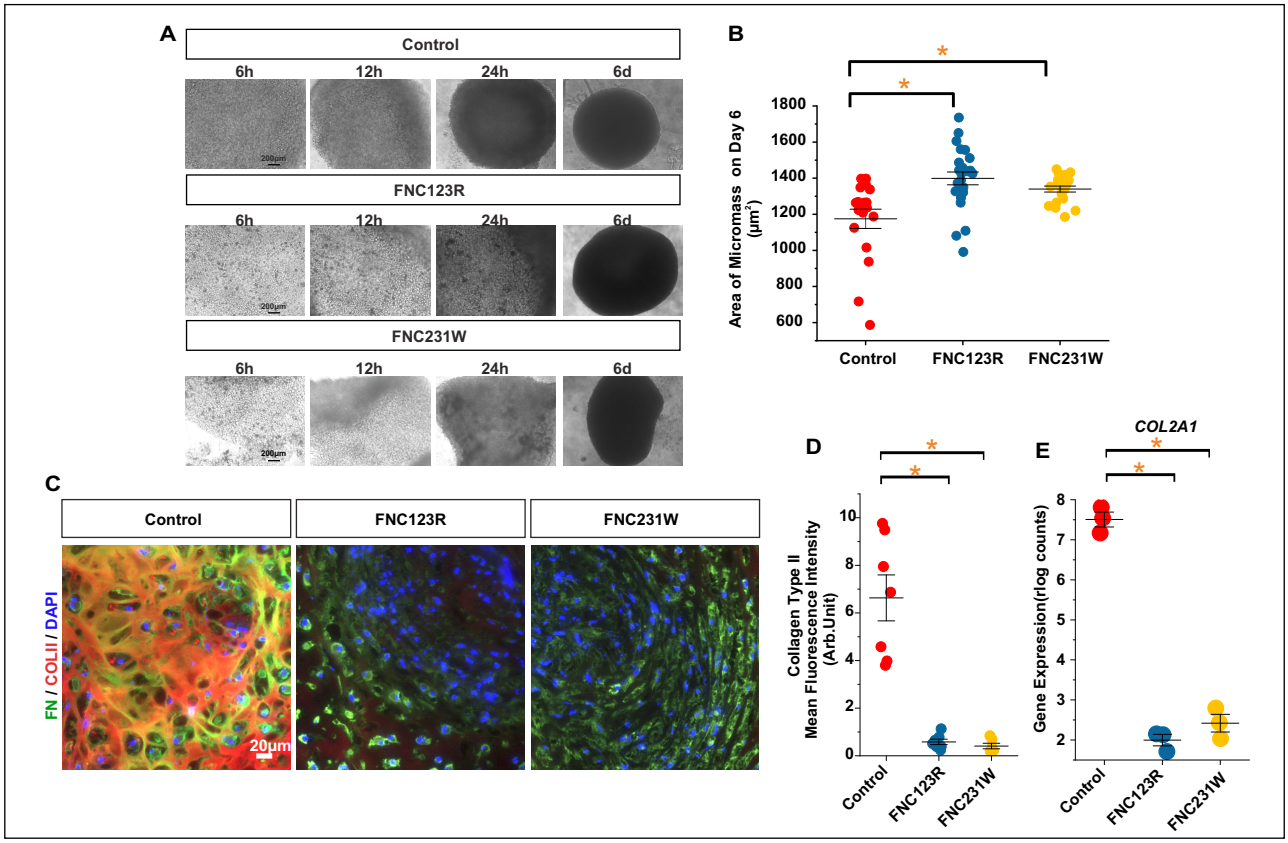
A
Control
6h
12h
24h
6d
FNC123R
FNC231W
B
Area of Micromass on Day 6 (μm²)
1800
1600
1400
1200
1000
800
600
Control
FNC123R
FNC231W
C
FN / COLII / DAPI
20μm
D
Collagen Type II Mean Fluorescence Intensity (Arb.Unit)
E
COL2A1
Gene Expression(rlog counts)

Figure 9

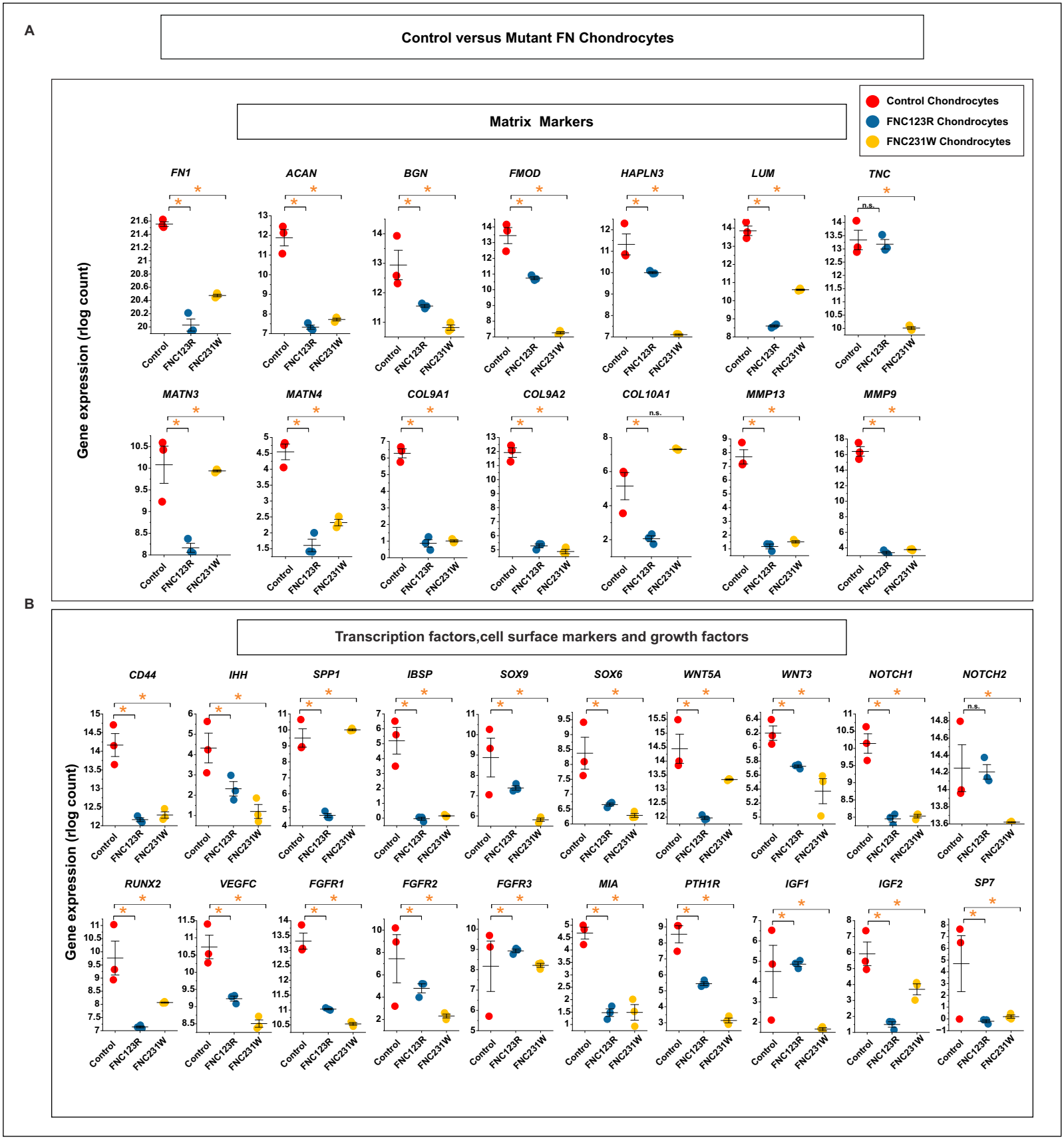
A
Control versus Mutant FN Chondrocytes
Matrix Markers
Control Chondrocytes
FNC123R Chondrocytes
FNC231W Chondrocytes
Gene expression (rlog count)
FN1
ACAN
BGN
FMOD
HAPLN3
LUM
TNC
MATN3
MATN4
COL9A1
COL9A2
COL10A1
MMP13
MMP9
n.s.
Control
FNC123R
FNC231W
B
Transcription factors,cell surface markers and growth factors
CD44
IHH
SPP1
IBSP
SOX9
SOX6
WNT5A
WNT3
NOTCH1
NOTCH2
RUNX2
VEGFC
FGFR1
FGFR2
FGFR3
MIA
PTH1R
IGF1
IGF2
SP7

Figure 10

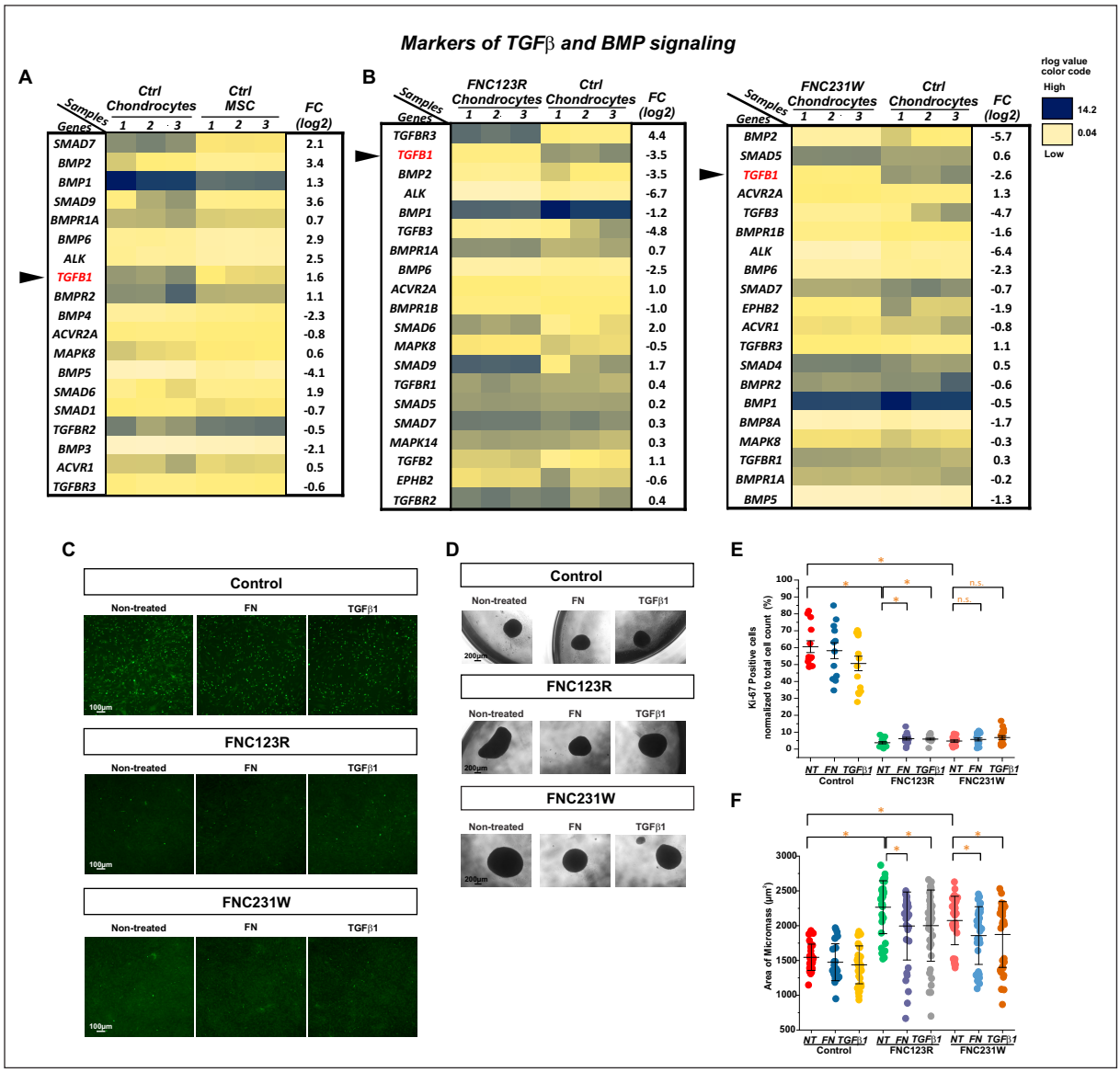
Markers of TGFβ and BMP signaling
A
Samples
Genes
Ctrl Chondrocytes
Ctrl MSC
1 2 3 1 2 3
FC (log2)
SMAD7 2.1
BMP2 3.4
BMP1 1.3
SMAD9 3.6
BMPR1A 0.7
BMP6 2.9
ALK 2.5
TGFB1 1.6
BMPR2 1.1
BMP4 -2.3
ACVR2A -0.8
MAPK8 0.6
BMP5 -4.1
SMAD6 1.9
SMAD1 -0.7
TGFBR2 -0.5
BMP3 -2.1
ACVR1 0.5
TGFBR3 -0.6
B
FNC123R Chondrocytes
Ctrl Chondrocytes
TGFBR3 4.4
TGFB1 -3.5
BMP2 -3.5
ALK -6.7
BMP1 -1.2
TGFB3 -4.8
BMPR1A 0.7
BMP6 -2.5
ACVR2A 1.0
BMPR1B -1.0
SMAD6 2.0
MAPK8 -0.5
SMAD9 1.7
TGFBR1 0.4
SMAD5 0.2
SMAD7 0.3
MAPK14 0.3
TGFB2 1.1
EPHB2 -0.6
TGFBR2 0.4
FNC231W Chondrocytes
Ctrl Chondrocytes
BMP2 -5.7
SMAD5 0.6
TGFB1 -2.6
ACVR2A 1.3
TGFB3 -4.7
BMPR1B -1.6
ALK -6.4
BMP6 -2.3
SMAD7 -0.7
EPHB2 -1.9
ACVR1 -0.8
TGFBR3 1.1
SMAD4 0.5
BMPR2 -0.6
BMP1 -0.5
BMP8A -1.7
MAPK8 -0.3
TGFBR1 0.3
BMPR1A -0.2
BMP5 -1.3
rlog value color code
High
14.2
0.04
Low
C
Control
Non-treated
FN
TGFβ1
100μm
FNC123R
FNC231W
D
200μm
E
Ki-67 Positive cells normalized to total cell count (%)
NT FN TGFβ1
Control
FNC123R
FNC231W
n.s.
F
Area of Micromass (μm²)

Figure 11

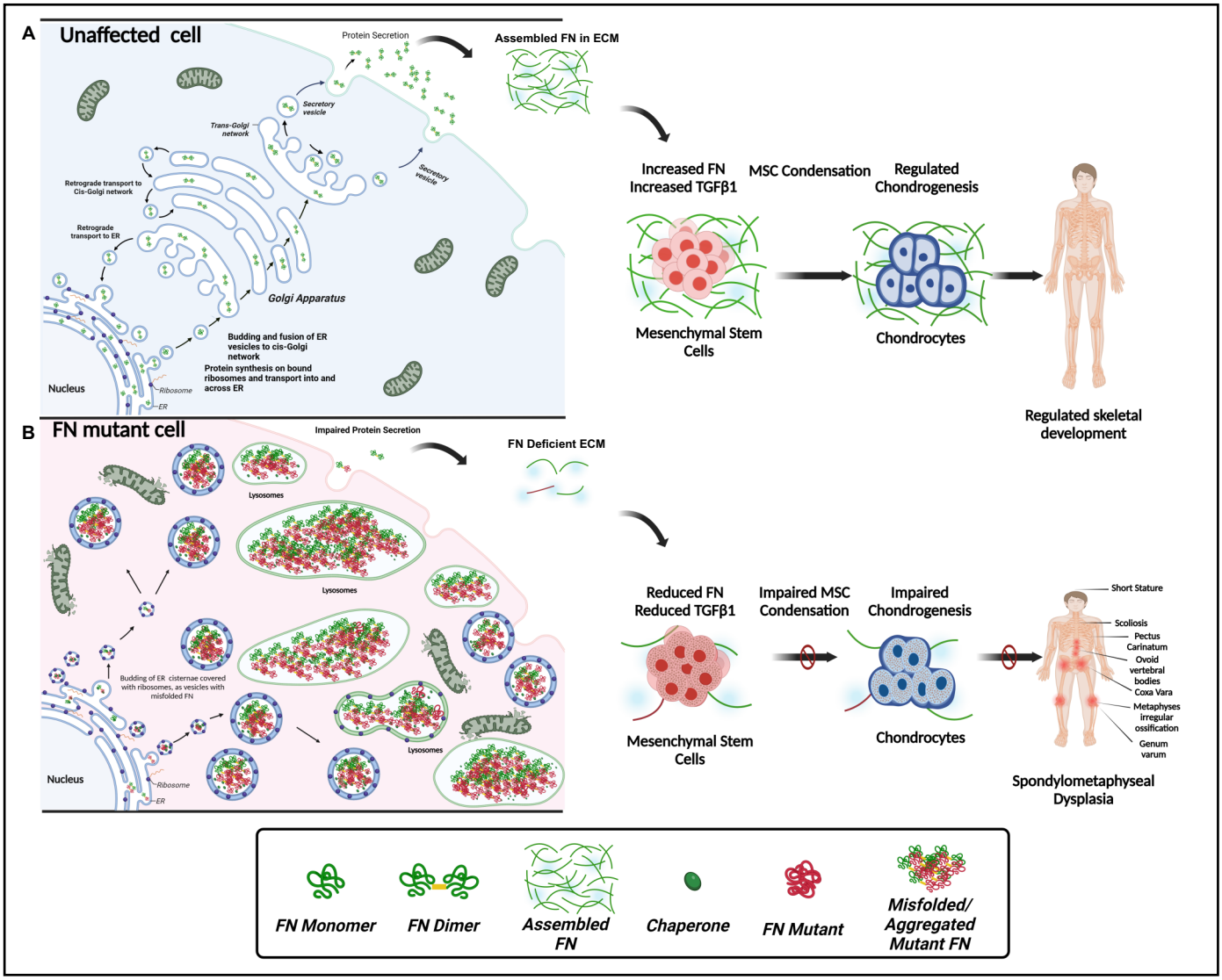
A
Unaffected cell
Protein Secretion
Assembled FN in ECM
Secretory vesicle
Trans-Golgi network
Retrograde transport to Cis-Golgi network
Retrograde transport to ER
Golgi Apparatus
Budding and fusion of ER vesicles to cis-Golgi network
Protein synthesis on bound ribosomes and transport into and across ER
Nucleus
Ribosome
ER
Increased FN
Increased TGFβ1
MSC Condensation
Regulated Chondrogenesis
Mesenchymal Stem Cells
Chondrocytes
Regulated skeletal development
B
FN mutant cell
Impaired Protein Secretion
FN Deficient ECM
Lysosomes
Budding of ER cisternae covered with ribosomes, as vesicles with misfolded FN
Nucleus
Ribosome
ER
Reduced FN
Reduced TGFβ1
Impaired MSC Condensation
Impaired Chondrogenesis
Mesenchymal Stem Cells
Chondrocytes
Short Stature
Scoliosis
Pectus Carinatum
Ovoid vertebral bodies
Coxa Vara
Metaphyses irregular ossification
Genum varum
Spondylometaphyseal Dysplasia
FN Monomer
FN Dimer
Assembled FN
Chaperone
FN Mutant
Misfolded/ Aggregated Mutant FN